Prograde infiltration of Cl-rich fluid into the granulitic continental crust from a collision zone in East Antarctica (Perlebandet, Sør Rondane Mountains)

Tetsuo Kawakami[1,*], Fumiko Higashino[1,2], Etienne Skrzypek[1], M. Satish-Kumar[3], Geoffrey Grantham[4], Noriyoshi Tsuchiya[5], Masahiro Ishikawa[6], Shuhei Sakata[1], Takafumi Hirata[1]

1 Department of Geology and Mineralogy, Graduate School of Science, Kyoto University, Kitashirakawa-Oiwake-cho, Sakyo-ku, Kyoto 606-8502, Japan

2 Research Fellow of Japan Society for the Promotion of Science

3 Department of Geology, Faculty of Science, Niigata University, 2-8050 Ikarashi, Nishi-ku, Niigata 950-2181, Japan

4 Department of Geology, University of Johannesburg, PO Box 524, Auckland Park, 2006, South Africa

5 Department of Geoscience and Technology, Graduate School of Engineering, Tohoku University, Aramaki, Aoba-ku, Sendai 980-9570, Japan

6 Graduate School of Environment and Information Sciences, Yokohama National University, Tokiwadai, Hodogaya-ku, Yokohama 240-8501, Japan

*Corresponding author; t-kawakami@kueps.kyoto-u.ac.jp

Abstract

Utilizing microstructures of Cl-bearing biotite in pelitic and felsic metamorphic rocks, the timing of Cl-rich fluid infiltration is correlated with the pressure-temperature-time (*P-T-t*) path of upper amphibolite- to granulite-facies metamorphic rocks from Perlebandet, Sør Rondane Mountains (SRM), East Antarctica. Microstructural observation indicates that the stable Al_2SiO_5 polymorph changed from sillimanite to kyanite + andalusite + sillimanite, and *P-T* estimates from geothermobarometry point to a counterclockwise *P-T* path characteristic of the SW terrane of the SRM. *In situ* laser ablation inductively coupled plasma mass spectrometry for U-Pb dating of zircon inclusions in garnet yielded ca. 580 Ma, likely representing the age of garnet-forming metamorphism at Perlebandet.

Inclusion-host relationships among garnet, sillimanite, and Cl-rich biotite (Cl > 0.4 wt%) reveal that formation of Cl-rich biotite took place during prograde metamorphism in the sillimanite stability field. This process probably predated partial melting consuming biotite (Cl = 0.1-0.3 wt%). This was followed by retrograde, moderately Cl-bearing biotite (Cl = 0.1-0.3 wt%) replacing garnet. Similar

timings of Cl-rich biotite formation in different samples, and similar $f(H_2O)/f(HCl)$ values of coexisting fluid estimated for each stage can be best explained by prograde Cl-rich fluid infiltration. Fluid-present partial melting at the onset of prograde metamorphism probably contributed to elevate the Cl concentration (and possibly salinity) of the fluid, and consumption of the fluid resulted in the progress of dehydration melting. The retrograde fluid was released from crystallizing Cl-bearing partial melts or derived externally. The prograde Cl-rich fluid infiltration in Perlebandet presumably took place at the uppermost part of the footwall of the collision boundary. Localized distribution of Cl-rich biotite and hornblende along large-scale shear zones and detachments in the SRM supports external input of Cl-rich fluids through tectonic boundaries during continental collision.

Keywords: fluid, brine, partial melting, Al_2SiO_5 polymorphs, chlorine, continental collision

Introduction

Low water activity fluids have been recognized as the major fluid species present under granulite facies conditions prevailing in the lower continental crust (Aranovich et al., 1987; Newton et al., 1998; Touret and Huizenga, 2011). Under such conditions, brines can immiscibly coexist with CO_2-rich fluids (Heinrich, 2007). Direct evidence of highly saline brine, such as fluid inclusions (van den Berg and Huizenga, 2001) and/or salt crystals (e.g., Markl and Bucher, 1998) have been reported, although

55 they are relatively uncommon. Rare preservation of brines as fluid inclusions is attributed to the low
56 viscosity and low wetting angle of brines (Watson and Brenan, 1987; Holness, 1997) that make it easy
57 for brine to escape the rock. In addition, steep isochores of NaCl-H_2O fluids in pressure-temperature
58 (*P*-*T*) space result in gross overpressurization of brine inclusions during heating and decrepitation or
59 implosion during isobaric cooling (Touret et al., 2016). These features probably hindered
60 understanding of the timing and spatial distribution of brines in high-grade metamorphic terranes.

61 The presence of Cl-rich biotite, hornblende and apatite is often taken as evidence for the presence
62 of Cl-bearing fluids and brines (e.g., Harlov and Förster, 2002; Higashino et al., 2013a; Safonov et al.,
63 2014). These minerals are known to incorporate Cl in place of OH in their crystal structures when they
64 exchange with Cl-bearing fluids (e.g., Munoz and Swenson, 1981; Kullerud, 1996). Data on Cl
65 partitioning between fluids and these minerals is available (e.g., Zhu and Sverjensky, 1991; 1992;
66 Mathez and Webster, 2005); the $f(H_2O)/f(HCl)$ ratio of the coexisting fluid can be estimated from the
67 composition of biotite and apatite (e.g., Selby and Nesbitt, 2000). In partially molten, migmatitic
68 pelitic gneisses, Cl-rich biotite may coexist with nanogranite/felsite inclusions (Kawakami et al.,
69 2016; see Hiroi et al. (2014) for 'felsite inclusions'), and thus not only subsolidus Cl-rich aqueous
70 fluid infiltration but also processes involving partial melting can lead to the formation of Cl-rich
71 biotite.

72 This study aims to correlate the reconstructed *P*-*T*-*t* path with partial melting and Cl-rich fluid

infiltration events using microstructural observations pointing to several stages of Cl-bearing biotite formation in pelitic and felsic gneisses from Perlebandet (western Sør Rondane Mountains (SRM), East Antarctica). We discuss multiple Cl-bearing fluid infiltration events in the SRM. Mineral abbreviations are after Kretz (1983).

Geological setting

The Sør Rondane Mountains

In the SRM (22º-28ºE, 71.5º-72.5ºS) of eastern Dronning Maud Land, East Antarctica (Fig. 1a), the granulite facies lower continental crust of a continental collision setting is widely exposed (Shiraishi et al., 1991; Asami et al., 1992). The SRM are thought to be a part of the collision zone between East and West Gondwana during the ca. 750–620 Ma 'East African-Antarctic Orogeny (EAAO)' (Jacobs et al., 2003) and are also affected by the ca. 570–500 Ma 'Kuunga Orogeny' (Meert, 2003). Apparent depositional ages of metacarbonate rocks from Balchenfjella, Brattnipene, Menipa and Tanngarden regions in the SRM (Fig. 1b) are estimated as late-Tonian and early-Cryogenian age (880–850 Ma and 820–790 Ma) based on a Sr isotope study (Otsuji et al., 2013). Protoliths of metacarbonates are considered to have been deposited in the Mozambique Ocean that separated the continental blocks that amalgamated to form Gondwana (Otsuji et al., 2013).

The SRM is divided into the NE and SW terranes which are separated by a gently N- to

NE-dipping mylonite zone named the Main Tectonic Boundary (MTB; Osanai et al., 2013) (Fig. 1b). The NE terrane is mainly composed of amphibolite- to granulite-facies metamorphic rocks of pelitic, psammitic, and intermediate compositions (Shiraishi and Kojima, 1987; Asami and Shiraishi, 1987; Grew et al., 1989) showing clockwise *P-T* paths (Osanai et al., 2013; Grantham et al., 2013). In contrast, the SW terrane is composed of granulite- to greenschist-facies rocks with a large volume of meta-tonalite (Fig. 1b; Shiraishi et al., 2008; Kamei et al., 2013), showing counterclockwise *P-T* paths (Adachi et al., 2013; Baba et al., 2013). U-Pb ages of detrital zircon are also different between these two terranes; detrital zircons older than 1200 Ma are absent from the SW terrane (Osanai et al., 2013; Kitano et al., 2016). Based on these observations, the two different *P-T* paths in these adjoining terranes are explained by the collision between these two terranes, with the NE-terrane thrusted over the SW-terrane during the EAAO at 650-600 Ma, followed by amphibolite-facies metamorphism at ca. 570 Ma (Osanai et al., 2013). A SE-dipping ductile extensional shear zone termed the Balchen Detachment Fault (BDF) structurally divides Balchenfjella (Fig. 1b), and the southeastward movement of the Berrheia unit (hanging wall side) with respect to the Gropeheia unit (footwall side) is inferred to represent an extensional deformation phase between ca. 600 Ma and ca. 549 Ma (Ishikawa et al., 2013), which is interpreted to result from extensional collapse after crustal overthickening.

The Main Shear Zone (Kojima and Shiraishi, 1986; Fig. 1b) that defines the boundary between older meta-tonalite and amphibolite-facies metamorphic rocks in the SW-terrane was inferred to have

109 limited tectonic significance by Osanai et al. (2013). However, Ruppel et al. (2015) interpreted it to be
110 a large-scale late Pan-African strike-slip structure of ca. 560-530 Ma, representing an important
111 lithotectonic boundary separating East African affinities from 'Indo-Antarctic' Rayner-age affinities
112 presumably close to the eastern margin of the EAAO (Ruppel et al., 2015).

113 The SRM is also interpreted to be a part of the hanging wall of a mega-nappe complex which
114 formed through continental collision between northern and southern Gondwana during the Kuunga
115 Orogeny at 580–540 Ma (Grantham et al., 2008; 2013), as supported by the data from part of the NE
116 terrane (Balchenfjella and Austhameren; Fig. 1b).

117 In the SRM, Cl-rich biotite, apatite and hornblende have been described in felsic and mafic
118 gneisses along the large scale shear zones and tectonic boundaries which extend over 200 km
119 (Higashino et al., 2013a; 2013b; 2015a; Fig. 1b). In eastern SRM (Balchenfjella; Fig. 1b), Cl-rich
120 biotite and apatite in pelitic gneisses have been interpreted to have resulted from interaction with a
121 Cl-rich fluid or melt that was present at near peak metamorphic condition of ca. 0.8 GPa and 800 ^{o}C
122 (Higashino et al., 2013a). In the central SRM (Brattnipene; Fig. 1b), Cl-rich hornblende and biotite are
123 formed along garnet-hornblende veins, and 'diffusion-like' profiles of Cl content in hornblende and
124 biotite decreasing from the vein towards the wall rock are observed (Higashino et al., 2015b). Mass
125 balance analysis revealed that elements mobile in brines rather than in melts were added to the wall
126 rock, suggesting that brine infiltration produced the garnet-hornblende veins in Brattnipene

(Higashino et al., 2015b).

In addition to these Cl-rich minerals in metamorphic rocks, magmatic hornblende and biotite show relatively high Cl contents in some granitoids in the SRM. Li et al. (2003, 2007) reported 0.28-0.32 wt.% Cl in hornblende from the Dufek granite, and 0.31-0.41 wt.% Cl in hornblende and 0.21-0.59 wt.% Cl in biotite from the Pingvinane granite (Fig. 1b). The U-Pb zircon age determined by SHRIMP or laser ablation inductively coupled plasma mass spectrometry (LA-ICPMS) is 619 ± 7 Ma (Li et al., 2006) and 637 ± 6 Ma (Elburg et al., 2016) for the Dufek granite, and 506 ± 4 Ma (Elburg et al., 2016) for the Pingvinane granite.

Perlebandet

Perlebandet is one of the westernmost nunataks in the SRM, where granulite facies layered gneisses are exposed (Fig. 1c). It is a key area to constrain the location of the MTB, and has been considered to belong to the NE terrane (Osanai et al., 2013) in the lack of detailed information of *P-T* path of this area. However, Perlebandet is interpreted to be part of the SW terrane on the basis of magnetic surveys (Mieth et al., 2014).

The main lithologies observed in Perlebandet are garnet-biotite (Grt-Bt) gneiss, garnet-sillimanite-biotite (Grt-Sil-Bt) gneiss, hornblende-biotite gneiss, marble and skarns, pyroxene granulite, and orthopyroxene-bearing amphibolite (Fig. 1c; Shiraishi et al., 1997). Previous SHRIMP

145 U-Pb zircon dating of a Sil-Grt-Bt gneiss from Perlebandet gave an inherited core age of 1009 ± 13
146 Ma, and rim ages of 736 ± 13 Ma, 609 ± 11 Ma, and 565 ± 7 Ma (Shiraishi et al., 2008). Among the
147 three rim ages, the latter two are considered as metamorphic, whereas the detrital or metamorphic
148 origin of the first one remains unclear (Shiraishi et al., 2008). Sillimanite is the most common
149 aluminosilicate mineral, and retrograde andalusite and kyanite are locally present (Kawakami et al.,
150 2010). Otsuji et al. (2013) reported low Sr and oxygen isotope ratios from Perlebandet
151 metacarbonates, which are not characteristic of continental settings. These low Sr isotope ratios can be
152 attributed to interaction with low Sr-bearing magmatic fluids or to the older depositional age of
153 Perlebandet metacarbonates compared to that from other parts of the SRM (Otsuji et al., 2013). Otsuji
154 et al. (2016) further pointed out that Nd and Sr isotopic data from metacarbonate rocks from
155 Perlebandet neither match the data from the rocks in the SW terrane, nor from the Balchenfjella in the
156 NE terrane. Based on these data, they proposed that Perlebandet carbonates were deposited in an
157 environment surrounding an isolated seamount in the Tonian to Cryogenian period, and that
158 amalgamation of Gondwana and the final closure of Mozambique Ocean and East Antarctic Ocean
159 took place at ca. 660-550 Ma (Otsuji et al., 2016).
160
161 **Analytical methods**
162 Quantitative analysis of rock-forming minerals and X-ray elemental mapping of thin section

163 samples were performed by a JEOL JXA-8105 superprobe. Analytical conditions for quantitative
164 analyses except for apatite were 15.0 kV acceleration voltage, 10 nA beam current, and 3 μm beam
165 diameter. The counting time for the peak and backgrounds was 30 s and 15 s for Cl, 60 s and 30 s for F,
166 and 10 s and 5 s for other elements. Analytical conditions for quantitative analysis of apatite followed
167 that recommended by Goldoff et al (2012). Natural and synthetic minerals (Astimex MINM25-53)
168 were used as standards and ZAF correction was applied. Analytical conditions for X-ray elemental
169 mappings were acceleration voltage of 15.0 kV, probe current of 50 nA, focused beam to 3 μm beam
170 diameter, and dwell time of 25-40 milliseconds. Electron microprobe analysis of rutile was also done
171 by a JEOL JXA-8105 superprobe, following analytical conditions recommended by Zack et al. (2004).
172 Cathodoluminescence (CL) images were obtained using a JEOL JXA-8105 superprobe equipped
173 with Hamamatsu Photonics high voltage power supply C9525 and photon counting unit C9744.
174 Analytical conditions for CL mapping were 15.0 kV acceleration voltage, 1 nA beam current, focused
175 beam to 10 μm beam diameter, and dwell time of 1 msec.
176 Minerals were also qualitatively identified by a Hitachi S3500H scanning electron microscope
177 equipped with an EDAX X-ray analytical system. Laser Raman spectroscopy (JASCO NRS 3100)
178 was used to identify Al_2SiO_5 minerals.
179 *In situ* zircon U-Pb dating on thin section samples via LA-ICP-MS was carried out using a Nu
180 Plasma II HR-MC-ICPMS coupled to a NWR femtosecond laser-ablation system. Backscattered

electron (BSE) and CL images were obtained prior to the analyses to identify spot positions, overlapping multiple growth zones, grain edges, cracks or damaged zircon grains. Detailed analytical conditions of the LA-ICP-MS analysis are given in Higashino et al. (2015a). Data were processed and plotted using *Isoplot 4.15* (Ludwig, 2012). All of the above analyses were done at the Department of Geology and Mineralogy, Graduate School of Science, Kyoto University.

Sample localities and sample descriptions

The samples used in this study are two Grt-Bt gneisses [samplesTK2009113001B (3001B) and TK2009112601C (2601C)] and three Grt-Sil-Bt gneisses [samples TK2009113001G (3001G), TK2009113001H (3001H) and TK2009112602D (2602D)] collected during the summer season of the 51st Japan Antarctic Research Expedition (JARE51; Tsuchiya et al., 2012). Samples were collected from the northern half of Perlebandet (Fig. 1c). The common Al_2SiO_5 mineral in these gneisses is sillimanite, found as inclusions in cores of garnet and as a matrix mineral defining the gneissose structure (Fig. 2a-d). A rare sample with strong retrogression (sample 3001G) contains secondary andalusite, kyanite, and sillimanite replacing garnet (Fig. 2e-n). Detailed descriptions of the samples studied are given below, and representative mineral analyses are given in Table 1.

Garnet-sillimanite-biotite gneiss (samples 2602D and 3001H)

These gneisses consist of garnet, sillimanite, biotite, K-feldspar, quartz and plagioclase (An19-23 in 2602D, and An13-17 in 3001H), and subordinate rutile, ilmenite, zircon, monazite and apatite. Muscovite is only present as a secondary mineral. Sillimanite is abundant in the matrix and also present as inclusions in cores of garnet (X_{Mg} = 0.25-0.29 in 2602D, and X_{Mg} = 0.25-0.32 in 3001H) (Fig. 2a). Biotite is not included in garnet. Garnet is replaced by secondary biotite at the rim and along the cracks. It does not preserve chemical zoning, except for the rims and along the cracks affected by the retrograde re-equilibration. The highest X_{Mg} content of garnet is preserved distant from the cracks where the retrograde effects are minimal. In both samples, sillimanite and biotite partly replace garnet rim. Retrograde biotite tends to have lower TiO_2 contents compared to matrix biotite. Cracks in garnet are filled with retrograde biotite with the lowest Cl (Cl ~ 0.01 wt.%) and the lowest TiO_2 (< 0.29 wt.%) contents.

In sample 2602D, garnet rim contain inclusions of quartz and K-feldspar. Matrix biotite has moderate Cl content (0.17-0.22 wt.%, X_{Mg} = 0.41-0.51) and the highest TiO_2 content (2.04-3.96 wt.%). Retrograde biotite (Cl < 0.15 wt.%, TiO_2 = 0.98-2.82 wt.%, X_{Mg} = 0.45-0.48) and plagioclase (An18-23) replace garnet at the rim (X_{Mg} = 0.11-0.13). Matrix sillimanite very rarely includes garnet (X_{Mg} = 0.23-0.24). Rutile in the matrix and that included in sillimanite gave Zr contents of 1125-1466 ppm (average = 1359 ppm; 8 points) and 1917-1947 ppm, respectively.

In sample 3001H, some sillimanite grains contain inclusions of green spinel. Biotite in this

sample has very low Cl content (Cl < 0.03 wt.%, X_{Mg} = 0.42-0.49) irrespective of its mode of occurrence. Garnet is replaced by biotite (Cl < 0.02 wt.%) and plagioclase (An16-18) at the rim (X_{Mg} = 0.10-0.12). Matrix sillimanite rarely includes rutile (Zr = 1473-1636 ppm). Rutile in the matrix has a Zr content of 1125-2162 ppm (average = 1712 ppm; 15 points).

Strongly retrogressed garnet-sillimanite-biotite gneiss (sample 3001G)

This is a folded, pelitic gneiss with sillimanite porphyroblasts (ca. 1cm in length). The matrix of this gneiss mainly consists of biotite, garnet, sillimanite, K-feldspar, plagioclase (An26-31), quartz and retrograde andalusite, kyanite, sillimanite and muscovite (Fig. 2b-n). K-feldspar is especially abundant in the matrix (Fig. 2e-f). Accessory minerals are ilmenite, zircon, monazite and rare rutile. Ti-oxide minerals are mostly ilmenite in the matrix, but rare rutile (Zr = 874-1273 ppm; average of 15 points = 1139 ppm) is preserved as inclusions in garnet (Fig. 2o) and in K-feldspar. Myrmekite is also present in the matrix. Garnet in this sample is strongly replaced mainly by biotite, plagioclase, andalusite, kyanite, and sillimanite (Fig. 2e-n).

Sillimanite is the only Al_2SiO_5 mineral included in garnet. Prismatic sillimanite porphyroblast in the matrix has an inclusion-poor core and inclusion-rich rim (Fig. 2b, c). Sillimanite porphyroblasts up to 1 cm in diameter show numerous subgrains and often includes smaller prismatic sillimanite with crystallographic orientations different from that of the host sillimanite (Fig. 2c). The core of

235 sillimanite porphyroblast includes plagioclase (An33-37), K-feldspar and moderately Cl-bearing
236 biotite (0.17-0.30 wt.%; Table 1). The rim of sillimanite can be recognized by the presence of
237 abundant inclusions of Zn-bearing spinel (ZnO = 4-6 wt.%, X_{Mg} [= Mg/(Mg+Fe_{total})] = 0.18-0.22),
238 plagioclase (An31-35), garnet (X_{Mg} = 0.18-0.19), biotite (Cl < 0.32 wt.%), ilmenite, and rare quartz
239 (Fig. 2c, d). Sillimanite that is replacing garnet (Fig. 2e, i, j) commonly includes Zn-bearing spinel
240 crystals, resembling the rim of prismatic sillimanite in the matrix. Randomly-oriented, fibrolitic
241 sillimanite is locally formed along the grain boundaries of matrix minerals.

242 Garnet is mostly xenomorphic, and includes sillimanite, Zn-bearing spinel, biotite, plagioclase,
243 quartz, ilmenite and zircon (Fig. 2k-n). It is replaced by retrograde minerals such as biotite, andalusite,
244 kyanite, sillimanite, muscovite, plagioclase and quartz (Fig. 2f-n). Replacement by biotite +
245 plagioclase intergrowths is also common (Fig. 2i-j). Garnet that locally includes Zn-bearing spinel
246 overgrows sillimanite porphyroblasts (Fig. 2b-d). Spinel included in such garnet is more Zn-rich than
247 that included in sillimanite. Garnet that overgrows sillimanite and separate garnet grains in the matrix
248 both show decreasing X_{Mg} from the core (X_{Mg} = 0.15-0.21) to the rim (X_{Mg} = 0.10-0.14). The X_{Ca} [=
249 Ca/(Fe+Mn+Mg+Ca)] slightly decreases towards the rim or remains constant at 0.04-0.07 (Table 1).
250 These garnet zonings are diffuse and are strongly affected by retrograde re-equilibration.

251 Biotite included in garnet-overgrowth on sillimanite (Fig. 2b) shows high Cl (< 0.41wt.% Cl) and
252 X_{Mg} (~ 0.63) and varying TiO_2 (2.3-6.0 wt.%) (Fig. 3a, b). Biotite included in sillimanite

253 porphyroblast shows moderate Cl contents (0.17-0.30 wt.%) with high X_{Mg} (0.46-0.56) and varying
254 TiO_2 (2.8-5.0 wt.%) (Fig. 3a, b). Matrix biotite shows moderate Cl contents (0.13-0.25 wt.%) with
255 lower X_{Mg} (~ 0.40) and moderate TiO_2 (2.5-3.6 wt.%) (Fig. 3a, b). Biotite in the biotite-plagioclase
256 intergrowth replacing garnet (Fig. 2g, i) shows moderate TiO_2 (3.2-4.2 wt.%) and Cl (0.17-0.24 wt.%)
257 contents and X_{Mg} (~ 0.47) value (Fig. 3a, b). Apparently retrograde, crack-filling biotite in garnet (Fig.
258 2k-n) shows moderate to low Cl (0.09-0.16 wt.%) and low TiO_2 (1.9-2.5 wt.%) contents (Fig. 3a, b).
259 Retrograde biotite developed at garnet rims also shows similar compositions to the crack-filling biotite
260 (Fig. 3a, b). There is a clear tendency for prograde biotites, such as inclusions in garnet and sillimanite
261 and some of the matrix biotite, to show Cl-rich composition and higher TiO_2 and X_{Mg} values than the
262 retrograde ones.

263 Andalusite intergrown with biotite commonly replaces garnet (Fig. 2f-e). Retrograde andalusite
264 is commonly accompanied by sillimanite and rare kyanite (Fig. 2e-n). Garnet is Fe-richer around the
265 andalusite-bearing replacement, and andalusite in the replacement locally includes irregularly-shaped
266 garnet and/or Zn-bearing spinel (Fig. 2k-n). Andalusite is never found as inclusions in garnet, and is in
267 contact with the matrix phases even when it is surrounded by garnet (Fig. 2k-n).

268 Kyanite is rare, and tends to be finer-grained than other Al_2SiO_5 polymorphs and is never found
269 as inclusions in garnet. It replaces garnet together with biotite, andalusite and sillimanite (Fig. 2g-j, m,
270 n). The CL images combined with laser Raman spectroscopy are useful in identifying dispersed

fine-grained kyanite because kyanite is more luminescent than sillimanite (moderately bright) and andalusite (dark) (Fig. 2g-j). Zn-bearing spinel is also found as inclusions in some kyanite grains.

The composition of Zn-bearing spinel included in all Al_2SiO_5 polymorphs and garnet varies from ZnO = 4.0-5.0 wt.% and X_{Mg} = 0.28 to ZnO = 11-13 wt.% and X_{Mg} = 0.18.

Garnet-biotite gneiss (sample 3001B)

This gneiss mainly consists of garnet, biotite, quartz, plagioclase and K-feldspar, with accessory zircon, ilmenite, fluorapatite and minor sulfide (Fig. 4a-c). Myrmekite is present in the matrix. Biotite included in garnet (Fig. 4a-c) shows high TiO_2 (3.5-7.3 wt.%) and moderate Cl (mostly 0.20-0.34 wt.%) contents and high X_{Mg} (~ 0.6) (Fig. 3c, d). Biotite in the matrix (Fig. 4a-c) has moderate TiO_2 (3.3-4.5 wt.%) and Cl (0.11-0.25 wt.%) contents and X_{Mg} of ~ 0.4 (Fig. 3c, d; Table 1). Retrograde biotite next to garnet, and crack-filling biotite in garnet (Fig. 4a-c) both show lower Cl contents below 0.21 wt.% (Fig. 3c, d). Some of the matrix biotite and retrograde biotites (in biotite-plagioclase intergrowths and retrograde biotite next to garnet) share the same chemical characteristics of having low TiO_2 and Cl contents and low X_{Mg} (Fig. 3c, d).

Garnet-biotite gneiss (sample 2601C)

This gneiss mainly consists of garnet, biotite, K-feldspar, quartz and plagioclase (Fig. 4d-f).

289 K-feldspar is abundant, and randomly-oriented secondary muscovite is present in the matrix.
290 Accessory minerals are zircon, ilmenite and fluorapatite. Minor sulfide is included in garnet and minor
291 myrmekite is locally present in the matrix. This sample has the most Fe-rich whole-rock composition
292 among the samples studied as suggested by the Fe-rich composition of mafic minerals (X_{Mg} of biotite
293 and garnet = 0.06-0.22; Table 1). Separate biotite grains in the matrix (Fig. 4d-f) show the highest Cl
294 contents (0.61-0.68 wt.%) and the highest X_{Mg} (~ 0.2) in this sample (Figs. 3e, 3f and 4d-f). Biotite
295 replacing garnet rim as biotite-plagioclase intergrowths (Fig. 4d-f) also show high X_{Mg} (~ 0.2) and
296 moderate to high Cl content (0.32-0.41 wt.%) (Fig. 3e, f). It shares the same chemical characteristics
297 as retrograde biotite near garnet. Crack-filling biotite in garnet (Fig. 4d-f) shows the lowest X_{Mg} and Cl
298 contents (Fig. 3e, f). No systematic variation in TiO_2 content (2.2-3.8 wt.%) is observed among
299 different biotite types in this sample (Fig. 3e, f).
300
301 **LA-ICPMS U-Pb zircon dating**
302 Zircon is commonly oval-shaped, and the diameter of zircon reported below represents the length
303 of the shorter axis. Weighted mean and lower intercept ages given below are at 95% confidence level.
304 Unless specified, ages reported below refer to $^{206}Pb/^{238}U$ results. A summary of the results of
305 LA-ICPMS U-Pb zircon dating is given in Supplementary Table 2.
306

Sample 3001G

Zircon in the matrix is commonly shorter than 100 μm in diameter, and shows oscillatory zoning (Fig. 5a-h). Analyses gave concordant U-Pb ages of ca. 1200-1100 Ma, 950-900 Ma, 750-700 Ma and 650-550 Ma. Ages older than 700 Ma are in most cases obtained from zircon cores, and the youngest ages of ca. 580 Ma are in most cases obtained from rims. Ages older than 900 Ma tend to have high Th/U ratios from 0.20 up to 1.1, while the younger age domains (750-550 Ma) give low Th/U ratios below 0.20 (Figs. 5a-h and 6a; Table 2). The weighted mean U-Pb age of zircon rims from matrix grains is 581 ± 10 Ma (n = 5, mean square of weighted deviates (MSWD) = 1.3, probability = 0.28).

Zircon included in garnet is commonly about 50 μm in diameter, and tends to have oscillatory zoned cores with bright- and dark-CL zones (Th/U = 0.01-0.40, mostly around 0.25), discordantly overgrown by dark-CL rims (Th/U = 0.01-0.03) (Fig. 5e, h). The lower intercept age for selected rim analyses of zircon included in garnet is 578 ± 9 Ma (n = 6, MSWD = 1.3, probability = 0.28), and Th/U ratios of these zircon rims with concordant ages are 0.04-0.07. Rim and mantle of a zircon grain included in the inclusion-rich rim of a sillimanite porphyroblast yielded 575 ± 13 Ma (n = 2, Th/U = 0.04-0.09) (Fig. 5g).

Zircon in the garnet breakdown microstructure of Cl-poor Bt + Ms ± And shows similar zoning to zircon included in garnet (Fig. 5a-d). The weighted mean U-Pb age of zircon rims (and mantles with similar age) in such microstructure is 573 ± 5 Ma (n = 9, MSWD = 0.83, probability = 0.57).

325

326 ***Sample 3001B***

327 Zircon in the matrix and zircon inclusions in garnet are commonly 30-70 μm in diameter, and
328 shares similar microstructural features. The inherited core and mantle of zircon show oscillatory
329 zoning under CL and BSE images, which are discordantly overgrown by relatively bright-CL rim
330 (Figs. 5i-l, 6b). Zircon in this sample yielded concordant U-Pb ages of 850-700 Ma and 630-550 Ma
331 (Fig. 6b). The youngest rim age from matrix zircon is 551 ± 14 Ma. Cores and rims of zircon included
332 in garnet gave 758-585 Ma. Among them, the weighted mean of rims is 596 ± 7 Ma (n = 4, MSWD =
333 0.74, probability = 0.53). Both in the matrix zircon and inclusion zircon in garnet, domains of ca. 600
334 Ma commonly correspond to the bright-CL rim, and show high Th/U ratios up to 1.6 (Fig. 5i, j).
335 However, some dark-CL parts with ca. 600 Ma age show relatively low Th/U ratios (0.05-0.38) (Fig.
336 5k).

337

338 ***Sample 2601C***

339 Zircon in the matrix and included in garnet are commonly 60-100 μm and 20-70 μm in diameter,
340 respectively (Fig. 5m-t). They share the same microstructural characteristics. The cores of zircon are
341 oscillatory zoned and bright under CL image, or unzoned and dark (Fig. 5m-t). Several-μm to ca. 10
342 μm thick, bright-CL rims are commonly developed (Fig. 5m-t except for 5o). The oscillatory zoned

343 cores tend to give older ages (> 600 Ma) than the unzoned dark-CL ones. Zircon in the matrix and
344 inclusions in garnet both show concordant U-Pb ages of ca. 600-550 Ma (Figs. 5m-t, 6c). The
345 weighted mean U-Pb age of the rims of zircon included in garnet is 583 ± 6 Ma (n = 17, MSWD = 1.14,
346 probability = 0.31). No significant difference is observed between the age distribution patterns of
347 matrix zircon and zircon inclusions in garnet. The Th/U ratios of zircon domains with 600-550 Ma
348 ages are mostly below 0.40 (Figs. 5m-t, 6d).
349
350 **Discussion**
351 ***Pressure-temperature path of the pelitic gneiss from Perlebandet***
352 Sample 3001G is strongly affected by retrograde metamorphism as suggested from the presence
353 of retrograde andalusite and kyanite. Therefore, it is suitable for constraining the retrograde
354 metamorphic *P-T* conditions. On the other hand, samples 2602D and 3001H are less affected by
355 retrograde overprint, and thus used to estimate peak metamorphic conditions.
356
357 ***1. Prograde to peak metamorphic conditions***
358 In all the sillimanite-bearing samples (3001G, 2602D and 3001H), sillimanite is commonly
359 found as porphyroblasts in the matrix, and is considered to have been stable during peak
360 metamorphism. The absence of prograde muscovite along the gneissose fabric together with the

361 presence of sillimanite + K-feldspar in the matrix suggest that peak metamorphic conditions exceeded
362 reaction (1)

363 $$Ms + Ab + Qtz \rightarrow Sil + Kfs + H_2O \text{ or melt.} \quad (1)$$

364 which was responsible for the formation of the core of sillimanite porphyroblasts in sample 3001G.
365 Sillimanite inclusions are abundant in garnet cores of samples 2602D and 3001H, and K-feldspar
366 is also abundant in the matrix. Sillimanite in the matrix of sample 3001G is partly to completely
367 overgrown by garnet (Fig. 2b-d), and some of the garnet overgrowths include Zn-bearing spinel grains
368 (Fig. 2b-d), suggesting consumption of the sillimanite rims that are hosting spinel to form garnet with
369 X_{Mg} = 0.10-0.20 (Fig. 7). Garnet with kyanite or andalusite inclusions is not seen in all studied
370 samples. These are consistent with the progress of reaction (Fig. 7)

371 $$Sil + Bt + Qtz \rightarrow Grt + Kfs + melt. \quad (2)$$

372 The absence of cordierite in all garnet-bearing felsic gneiss samples suggests that the *P-T* conditions
373 did not exceed the reaction

374 $$Bt + Sil + Qtz \rightarrow Grt + Crd + Kfs + melt. \quad (3)$$

375 Garnet, plagioclase, biotite and rare quartz are included in the inclusion-rich rim of a sillimanite
376 porphyroblast in sample 3001G (Fig. 2b-d). The composition of biotite and garnet separately included
377 in sillimanite (Table 1) are most likely to preserve compositions of entrapment, because sillimanite
378 would hinder Fe-Mg exchange reactions between garnet and biotite after entrapment. Therefore,

379 prograde *P-T* conditions can be estimated using these minerals. The Grt-Bt (GB) geothermometer
380 (Holdaway et al., 1997; Holdaway, 2000) and the garnet-Al_2SiO_5-quartz-plagioclase (GASP)
381 geobarometer (Holdaway, 2001) yielded ca. 700 ºC, 0.47 GPa, which is in agreement within error of
382 the geothermobarometry (± 50 ºC and ± 0.10 GPa) with *P-T* conditions of reaction (2) for the observed
383 garnet composition of X_{Mg}^{Grt} = 0.10-0.20 in the NaKFMASH system (Fig. 7). The rarity of quartz
384 inclusions in the sillimanite rims may imply local absence of quartz, in which case the result may
385 represent the highest-*P* estimate. Although the Grt-Bt thermometer of Holdaway (2000) does not
386 account for the effects of F and Cl, calculations using the Zhu and Sverjensky (1992) calibration
387 showed that the opposing effects of F (*T* increase) and Cl (*T* decrease) on the temperature estimate
388 canceled each other out, and thus the effects of F and Cl are negligible in this sample.

389 On the other hand, the absence of a significant low-*P* retrograde overprint in samples 2602D and
390 3001H suggests that such rocks preserve peak metamorphic conditions better. In these samples, garnet
391 core with sillimanite inclusions (Fig. 2a) and matrix plagioclase core are interpreted as coexisting with
392 sillimanite and quartz, and used in the GASP geobarometry (Holdaway, 2000). For peak temperature
393 estimate, Zr-in-rutile thermometry (Zack et al., 2004; Tomkins et al., 2007) was applied to rutile
394 included in sillimanite and that in the matrix. The Tomkins et al. (2007) calibration is preferred in this
395 study since it takes pressure effect into account and is experimentally calibrated. Peak *P-T* conditions
396 estimated by the intersection of Zr-in-rutile thermometry (Tomkins et al., 2007) and GASP

397 geobarometry (Holdaway, 2001) are ca. 768-840 ºC and 0.8-1.0 GPa. The Grt-Bt geothermometry is
398 considered less reliable than the Zr-in-rutile thermometry in this case, because the X_{Mg} of matrix
399 biotite or inclusion biotite in garnet is more susceptible to retrograde re-equilibrium compared to rutile
400 included in sillimanite. The peak *P-T* conditions above are consistent with those of reaction (2) for
401 garnet with composition of $X_{Mg}^{Grt} \sim 0.40$, higher than that observed at the sillimanite-bearing garnet
402 core (Table 1; Fig. 7), implying a modification of X_{Mg} of garnet during retrograde metamorphism.
403 Sample 3001G, affected by the low-*P* retrograde overprint, also preserves rutile as inclusions in
404 garnet and K-feldspar or rarely in the matrix (Fig. 2o). The Zr-in-rutile thermometry gives temperature
405 estimates (743-780 ºC assuming 1.0 GPa) almost consistent with those of samples 2602D and 3001H.
406 This observation strongly supports that sample 3001G shared the same peak *P-T* conditions as other
407 samples before the low-*P* retrograde overprint.
408
409 ***2. Retrograde metamorphic conditions and proposed P-T path***
410 In sample 3001G, peak garnet is commonly replaced by three Al_2SiO_5 polymorphs (Fig. 2i-j, m-n).
411 It is difficult to define the sequence of andalusite and kyanite formation from their microtextures (Fig.
412 2g-j, m-n). Some sillimanite grains surrounding retrogressed garnet and including Zn-bearing spinel
413 grains in sample 3001G (Fig. 2i) may have been originally included in garnet and survived the garnet
414 breakdown reactions, because Zn-bearing spinel inclusions are the typical feature for prograde

415 sillimanite rims (Fig. 2b, c). However, the coexistence of andalusite+sillimanite, andalusite+kyanite,
416 and andalusite+kyanite+sillimanite in the replacement microtextures of garnet suggests garnet
417 breakdown near the *P-T* conditions of the Al_2SiO_5 triple point. Since the coexistence of three Al_2SiO_5
418 polymorphs in the garnet breakdown microstructure is only preserved in sample 3001G, it is likely that
419 localized fluid infiltrated this sample at *P-T* conditions of the Al_2SiO_5 triple point to trigger the
420 retrograde reaction. This is also supported by the GASP geobarometry (Holdaway, 2000) and the
421 Grt-Bt geothermometry (Holdaway et al., 1997; Holdaway, 2000) using mineral compositions of the
422 breakdown microstructure of garnet into biotite, plagioclase, quartz and Al_2SiO_5 minerals, which yield
423 *P-T* conditions of ca. 600 °C and 0.48 GPa, close to the Al_2SiO_5 triple point (Fig. 7). The almost
424 complete cancelation of the opposite effects of F and Cl in biotite on the Grt-Bt geothermometer is
425 confirmed by using Zhu and Sverjensky (1992) calibration, supporting the above *P-T* estimate. Since
426 prograde (ca. 700 °C, 0.47 GPa) and retrograde (ca. 600 °C, 0.48 GPa) *P-T* conditions are estimated
427 using the same geothermobarometers, and since the effects of F and Cl in biotite can be ignored, we
428 consider the differences between them meaningful. Therefore, by connecting prograde, peak and
429 retrograde *P-T* estimates from three samples, a counterclockwise *P-T* path for the Perlebandet rocks is
430 proposed (Fig. 7).

431 Garnet rims are also locally replaced by the intergrowth of biotite and plagioclase in all samples.
432 Utilizing the composition of garnet rims and biotite and plagioclase in the intergrowth, and applying

433 the Grt-Bt geothermometer (Holdaway et al., 1997; Holdaway, 2000) and the
434 garnet-biotite-plagioclase-quartz (GBPQ) geobarometer (Wu et al., 2004), retrograde *P-T* conditions
435 of garnet breakdown to biotite + plagioclase are estimated. These vary depending on samples, and are
436 ca. 580 ºC and ca. 0.40 GPa for sample 3001G (average of 4 estimates; Fig. 7), ca. 640 ºC, 0.66 GPa
437 for sample 3001B (average of 5 estimates; Fig. 7), and ca. 760 ºC, ca. 0.97 GPa for sample 2601C
438 (average of 5 estimates; Fig. 7). Among these, an estimate from sample 3001G is consistent with the
439 estimate by the GB-GASP pair (Fig. 7). These *P-T* conditions are consistent with the proposed
440 counterclockwise *P-T* path (Fig. 7).

441 This proposed *P-T* path is very similar to that estimated for Brattnipene, central SRM (Fig. 1b;
442 e.g., Adachi et al., 2013; Baba et al., 2013), suggesting that Perlebandet belongs to the SW terrane of
443 the SRM (Fig. 1b; e.g., Mieth et al., 2014). Our results of zircon dating (Fig. 6) are consistent with
444 previous results from Perlebandet (Shiraishi et al.. 2008) in that detrital ages older than 1200 Ma are
445 absent. This is also true for SW terrane rocks of the SRM (Osanai et al., 2013), and thus zircon data
446 also support Perlebandet as being part of the SW terrane (Fig. 1b).

447

448 ***Timings of Cl-bearing fluid infiltration and relationship with partial melting***

449 The presence of Cl-rich biotite has been considered as evidence for the presence of brines (e.g.,
450 Newton et al., 1998; Manning and Aranovich, 2014; Safonov et al. 2014). Although the $f(H_2O)/f(HCl)$

451 ratio of the coexisting fluid can be deduced from the composition of biotite and apatite (e.g., Selby and
452 Nesbitt, 2000), it should be noted that the salinity of the fluid cannot be directly determined by this
453 method (e.g., Rubenach, 2005). However, if the fluid coexists with silicate melt, the HCl concentration
454 can be related to the total Cl concentration in the fluid by the equation $\log(HCl/\Sigma Cl)^{aq} =$
455 -0.63-0.00035*P (bars) up to 0.67 GPa (Piccoli and Candela, 1994). This means that at pressures
456 typical of the middle crust, most of the Cl forms complexes with cations other than H. Therefore,
457 considering a case where Cl-bearing fluid coexists with melt, low $f(H_2O)/f(HCl)$ ratios in the fluid
458 indicates abundant chloride salts in the fluid (i.e., high salinity). It is important, therefore, to carefully
459 consider the melt-related processes that can increase Cl contents in biotite in addition to fluid-related
460 processes. Several possible mechanisms to elevate Cl-contents in biotite are listed below, and their
461 likeliness is discussed:

462 (a) Original Cl-rich whole-rock compositions allowed biotite to become Cl-rich.

463 (b) Consumption of originally Cl-bearing biotite through melting reactions caused an increase
464 of Cl-content in remaining biotite.

465 (c) Retrograde consumption of H_2O by hydration reactions increased Cl content in the fluid,
466 resulting in the increase of Cl in coexisting biotite (Kullerud, 1996; Markl and Bucher,
467 1998).

468 (d) Subsolidus Cl-rich fluid infiltration occurred (e.g., Newton et al., 1998; 2014; Higashino et

469 al., 2015b).

470 (e) Infiltration of Cl-rich fluid triggered anatexis, and preferential partitioning of H_2O into the
471 melt resulted in enrichment of Cl in the fluid (e.g., Aranovich et al., 2013; Safonov et al.,
472 2014).

473 Cases (a)-(c) assume closed system behavior of Cl, and (d)-(e) assume open system behavior of Cl.
474 Case (b) plays an important role if the partition coefficient of Cl between granitic melt and biotite is
475 greater than 1. Based on experiments at 0.2 GPa, D_{Cl}(biotite/melt) is estimated to be ~1 to 6
476 (Icenhower and London, 1997). Recently, Safonov et al. (2014) performed a melting experiment of a
477 biotite-amphibole gneiss with H_2O-CO_2-(K, Na)Cl fluids at 0.55 GPa and 750-800 °C. Their
478 compositional data of coexisting biotite (X_{Mg} = 0.43-0.57) and melt imply that Cl is preferentially
479 incorporated in the melt rather than in biotite, that is, D_{Cl}(biotite/melt) is less than 1 at 0.55 GPa and
480 800 °C. Therefore, the behavior of Cl under middle crustal depths can be different from that in shallow
481 levels of the crust, and if this is the case, case (b) alone is not likely a strong process to elevate Cl
482 content in biotite, at least for samples 3001B and 3001G having X_{Mg} values of biotite (X_{Mg} =
483 0.40-0.64; Table 1) similar to the experiment of Safonov et al (2014).

484 Sample 3001G preserves Cl-rich biotite (~ 0.4 wt.%) as inclusions in garnet. Biotite inclusions in
485 garnet tend to re-equilibrate and change X_{Mg} on cooling, while preserving their original halogen
486 content. Biotite was already Cl-rich prior to the garnet-formation by reaction (2), because moderately

487 Cl-bearing biotite (< 0.30 wt.%Cl) is included in sillimanite porphyroblasts predating garnet
488 formation (Fig. 3a). Biotite inclusions in garnet from sample 3001B show the highest Cl-content in the
489 sample, suggesting prograde formation of Cl-enriched biotite (Fig. 3b). Therefore, case (c) can be
490 ruled out. Although case (a) cannot be ruled out, we consider that the similar timing of Cl-enriched
491 biotite formation in different lithologies can be best explained by the infiltration of a Cl-rich fluid. The
492 $\log[f(H_2O)/f(HCl)]$ and $\log[f(H_2O)/f(HF)]$ values of the fluid estimated assuming its presence during
493 prograde stage for these two samples are in good agreement (Table 1), supporting the infiltration of
494 fluids with a similar composition. External input of Cl-rich fluid is also supported by the localized
495 field distribution of Cl-rich minerals in the SRM as discussed in the next section.

496 At *P-T* conditions estimated for reaction (2) in Perlebandet (~700 ºC and ~0.5 GPa), aH_2O of a
497 pelitic gneiss undergoing partial melting can be estimated to be ~ 0.85 (Clemens and Vielzeuf, 1987).
498 Ascribing this lowering of aH_2O to the addition of NaCl and KCl, XH_2O is estimated to be ~ 0.9
499 using the aH_2O-XH_2O relationship by Aranovich and Newton (1997), corresponding to ~ 26 wt%
500 NaCl (KCl). This is the highest estimate of salinity of the fluid, because CO_2 can also contribute to
501 lower aH_2O. It is difficult, however, to envisage source of the voluminous high-salinity fluid. More
502 likely case is an infiltration of smaller volume of lower salinity fluids that continually increased
503 salinity through preferential partitioning of H_2O into anatectic melts (Aranovich et al., 2013). In such
504 case, we may assume that the fluid-present reaction such as follows (e.g., Yardley and Barber, 1991)

505 took place prior to the dehydration melting reaction (2),

506 $Bt + Sil + Kfs + Qtz + H_2O \rightarrow$ melt (4).

507 As fluid-present melting reaction proceeds by consuming H_2O, $\log[f(H_2O)/f(HCl)]$ and

508 $\log[f(H_2O)/f(HF)]$ values of the fluid will decrease, resulting in an increase of Cl content in biotite.

509 Small volume of the fluid will be soon used up, resulting in cessation of the fluid-present partial

510 melting reactions, and further melting must proceed by dehydration melting reactions (e.g., Brown,

511 2013) such as reaction (2) in the present case. The escape of concentrated fluids from the system with

512 the assistance of deformation or low wetting angle of brines will also help switching the reaction

513 from fluid-fluxed melting to dehydration melting. This process might explain why the Cl content of

514 biotite included in peritectic garnet formed by dehydration melting reaction (2) is higher than that

515 included in sillimanite porphyroblasts (Figs. 2b-d and 3).

516 On the other hand, some fluid-present melting reactions can also produce peritectic phases as

517 sillimanite and garnet (Weinberg and Hasalová, 2015). Reactions such as

518 $Ms + Pl + Qtz + H_2O \rightarrow Sil + Bt +$ melt (5)

519 and

520 $Bt \pm Crd + Sil + Pl + Qtz + H_2O \rightarrow Grt \pm Kfs +$ melt (6)

521 (Jung et al., 2000; Milord et al., 2001) are the examples reported to occur at the *P*-*T* conditions for the

522 beginning of partial melting in this study (~ 0.5 GPa and ~ 700 °C). At medium pressure of ~ 0.5 GPa,

523 fluid-present melting and dehydration melting reactions take place in relatively small temperature
524 intervals. However, observed mineral compositions and sequences of reactions are mostly consistent
525 with the *P-T* diagram constructed under the scheme of dehydration melting (Fig. 7). This might
526 suggest that fluid-present melting occurred in the Perlebandet rocks only at the onset of the prograde
527 partial melting process, and the subsequent melting occurred through dehydration melting reactions.
528 In sample 3001G, matrix biotite as a remnant of reaction (2) was presumably once Cl-rich.
529 Compositional similarity between matrix biotite and microstructurally secondary biotite (Fig. 3)
530 suggests that moderately Cl-bearing matrix biotite is a result of recrystallization of former Cl-rich
531 biotite, re-equilibrated with retrograde fluids possibly released from the crystallizing melt. Using the
532 *P-T* conditions of retrograde metamorphism, $\log[f(H_2O)/f(HCl)]$ of the retrograde fluid can be
533 estimated as 4.2-4.3, with an average of 4.3 (Table 1).
534
535 ***The age of metamorphism and Cl-rich fluid infiltration***
536 In sample 3001G, rims of matrix zircon and inclusion zircon in garnet and sillimanite all yielded
537 U-Pb ages of 580-575 Ma. Most of these zircon rims show Th/U ratios below 0.1 (Fig. 6d), typical for
538 metamorphic zircon (e.g., Rubatto, 2002). The garnet-forming reaction was probably partial melting
539 reaction (2). Therefore, garnet-forming, sillimanite-grade metamorphism is likely to have occurred at
540 or after ca. 580 Ma, together with the Cl-rich fluid infiltration. Moderately Cl-bearing biotite replacing

541 garnet suggests that Cl-bearing aqueous fluid was present during retrograde garnet breakdown. The
542 weighted mean U-Pb age of rims of zircon found in the microstructure of garnet replaced by Al_2SiO_5
543 minerals and biotite is 573 ± 5 Ma. The similarity of this age with zircon rims included in garnet
544 implies that the retrogression took place soon after the peak metamorphism, or zircon was inert during
545 the retrograde breakdown of garnet.

546 Samples 3001B and 2601C both give constraints that are consistent with the above scenario. For
547 sample 3001B, the formation of garnet and moderately Cl-bearing biotite included in it (Fig. 3e, f) was
548 presumably at 596 ± 7 Ma or younger. The fluid at retrograde stage shows $\log[f(H_2O)/f(HCl)]$ value of
549 4.0-5.0, with an average of 4.5 (Table 1). For sample 2601C, garnet growth would predate or coincide
550 with 583 ± 6 Ma. Low Th/U zircon rims (Fig. 6d) supports this to be the metamorphic age. Markedly
551 high Cl concentration of isolated matrix biotite in this sample (Cl > 0.61 wt.%) reflects Mg-Cl
552 avoidance, in addition to the Cl-rich nature of the coexisted fluid, since biotite in this sample is
553 Fe-richer than other samples (Fig. 3). The $\log[f(H_2O)/f(HCl)]$ of the near-peak to retrograde fluid is
554 calculated as 3.5-4.2, with an average of 3.9 (Table 1).

555 To summarize, the timing of garnet-forming prograde metamorphism in Perlebandet is estimated
556 to be ca. 580 Ma or younger. Since biotite was already enriched in Cl before the onset of reaction (2),
557 the formation of highly to moderately Cl-bearing biotite in samples 3001G and 3001B took place
558 before or at ca. 580 Ma during prograde metamorphism. Taking into account that estimated prograde

559 log[f(H_2O)/f(HCl)] and log[f(H_2O)/f(HF)] of fluid are almost the same among the samples studied, it is
560 likely that external Cl-bearing fluid infiltration occurred, prior to or simultaneously with the
561 sillimanite-forming reaction. On the other hand, the presence of a retrograde, Cl-bearing fluid with
562 log[f(H_2O)/f(HCl)] = 4.0-5.0 (with one exception of 3.5) is detected from three samples. This probably
563 lasted until ca. 550 Ma. During the retrograde decompression, log[f(H_2O)/f(HCl)] of fluids increased
564 slightly or was almost constant (Table 1; Fig. 7).

565 At the outcrop scale, fluid pathways may be localized (e.g., Aranovich et al., 2010; Dubinina et
566 al., 2015; Kusebauch et al., 2015). This is also suggested in the SRM by localized distribution of
567 post-peak Cl-rich veins in the outcrop scale in Brattnipene (Fig. 1b; Higashino et al., 2015b). The
568 localized distribution of prograde Cl-bearing biotite in Perlebandet shows that Cl-bearing fluid
569 pathways may be localized during prograde metamorphism as well, but obscured by later ductile
570 deformation.

571

572 ***Comparison with other areas of the SRM***

573 The *P-T-t* conditions of Cl-rich aqueous fluid infiltration in the SRM have been previously
574 determined from two other localities; the eastern part (Balchenfjella; Higashino et al., 2013a) and the
575 central part (Brattnipene; Higashino et al., 2015a) (Fig. 1b). In Balchenfjella, the *P-T* conditions of
576 Cl-rich biotite and apatite entrapment in the garnet rim are estimated to be ca. 800°C and 0.80 GPa at

577 603 ± 14 Ma, which corresponds to the early retrograde stage postdating a peak metamorphic event at
578 ca. 850ºC and 1.1 GPa (Higashino et al., 2013a). A subsequent Cl-poor fluid infiltration is recorded in
579 Cl-poor matrix biotite, and estimated to have occurred at 564 ± 17 Ma from the rim age of zircon in the
580 matrix (Higashino et al., 2013b). On the other hand, in Brattnipene, early retrograde Cl-rich fluid
581 infiltration is estimated at ca. 700 ºC, 0.75 GPa and after ca. 620 Ma (Higashino et al., 2015b). In
582 contrast to these post-peak Cl-rich fluid activities, the present study shows that the Cl-rich biotite
583 included in garnet was formed during prograde metamorphism possibly as a result of Cl-bearing fluid
584 infiltration. External input of Cl-rich fluid during prograde- to peak-metamorphism possibly produced
585 Cl-bearing partial melt, and its crystallization during decompression and cooling resulted in a release
586 of post-peak, Cl-bearing fluid (Fig. 7).

587 Experimental data by Safonov et al. (2014) shows that melt can contain more Cl than coexisting
588 biotite at 0.55 GPa and 750-800 ºC. The fluid released by the crystallization of such melt would have
589 significantly more Cl than coexisting melt (Webster, 1992; Aranovich et al., 2013). Therefore, one
590 possible mechanism to produce Cl-rich fluid during the retrograde stage is the crystallization of
591 Cl-bearing partial melt. However, if the partial melting and crystallization of the melt alone is the
592 cause of Cl-rich fluid, Cl-rich biotite should be more widely distributed throughout the NE terrane of
593 the SRM where partially molten granulites and migmatites are widely distributed (Fig. 1b). What is
594 actually observed in the field is the localized distribution of Cl-rich biotite and hornblende along

595 large-scale shear zones and detachments both in felsic and mafic gneisses (Fig. 1b; Higashino et al.,
596 2015a). The distribution of Cl-rich minerals corresponds with the boundaries of magnetic anomaly
597 domains of Mieth et al. (2014). This trend may be obscured by a possible granite intrusion near
598 Perlebandet that is inferred to be the source of a high-magnetic anomaly (Mieth et al., 2014), but
599 ignoring the possible effect of this granite intrusion, Perlebandet is also located along the boundaries
600 of magnetic anomaly domains which corresponds to the major tectonic boundaries (e.g., Mieth et al.
601 2014). These suggest that the input of Cl in the SRM including Perlebandet is probably external,
602 possibly as Cl-rich fluid infiltration channeled along the tectonic boundaries (e.g., Glassley et al.,
603 2010) during prograde metamorphism. One occurrence of Cl-rich biotite in Brattnipene is at a major
604 shear zone containing peridotite and pyroxenite lenses (Fig. 1b; location 4 of Higashino et al. 2013),
605 supporting this idea. Because Perlebandet and Brattnipene share the counterclockwise *P*-*T* paths, they
606 should both belong to the footwall side of the MTB based on the tectonic model by Osanai et al. (2013)
607 (Fig. 8). Therefore, the Cl-rich fluid infiltration presumably took place at the uppermost part of the
608 footwall of the MTB (Fig. 8).

609 Based on this tectonic constraint, there are several candidates for the origin of the Cl-rich fluids.
610 Because the Mozambique Ocean is considered to have been located between the NE and SW terranes
611 of the SRM before collision (Otsuji et al., 2016), sea water introduced into the depth and fluids
612 released from the mantle are the likely candidates, and should be examined in future studies. High Cl

613 content in biotite, hornblende and apatite is a measure of low log[f(H_2O)/f(HCl)] of fluids, implying
614 that the origin of Cl-rich fluids in the SRM can be also related to the magmatic activity during
615 collision.

616 Multiple episodes of zircon growth within single orthogneissic samples from the NE terrane with
617 ages from ca. 630 Ma to ca. 535 Ma described by Grantham et al. (2013) and the result of this study
618 from the SW terrane indicate a long history of metamorphism, magmatism and deformation that
619 affected both terranes (e.g., Elburg et al., 2016), and multiple Cl-rich fluid infiltrations took place in
620 the SRM during this period (e.g., Higashino et al., 2013; 2015a).

621

622 **Conclusion**

623 Chlorine-rich fluid infiltration into the upper-amphibolite- to granulite-facies middle continental
624 crust at the prograde stage of counterclockwise *P*-*T* path is likely at Perlebandet (western SRM, East
625 Antarctica). This presumably occurred in the uppermost part of the footwall of the continental
626 collision boundary at ca. 580 Ma. The localized distribution of Cl-rich biotite and hornblende along
627 large-scale shear zones and detachments in the SRM supports the external input of Cl-rich fluids
628 through tectonic boundaries during continental collision.

629

630 **Acknowledgements**

We would like to thank R.C. Newton and L.Y. Aranovich for constructive reviews that helped improving the manuscript and M. Scambelluri for editorial efforts. D. van Reenen is thanked for critical comments on the previous version of the manuscript. Members of JARE and Nishi-Higashi seminar are thanked for fruitful discussions and supports during the field work in the SRM. Kota Takatsuka and Kentaro Hattori are thanked for assistance during LA-ICPMS analyses. This study was financially supported by the JSPS KAKENHI Grant Number 26400513 and the NIPR General Collaboration Project (No.25-14) to T. Kawakami, and Grant-in-Aid for JSPS Fellows (No. 25・715) to F. Higashino.

References

Adachi, T., Hokada, T., Osanai, Y., Nakano, N., Baba, S., Toyoshima, T., 2013. Contrasting metamorphic records and their implications for tectonic process in the central Sør Rondane Mountains, eastern Dronning Maud Land, East Antarctica. In: Harley SL, Fitzsimons LCW, Zhao Y (ed) Antarctica and Supercontinent Evolution. Geological Society, London, Special Publication 383, 113-133.

Aranovich, L.Y., Shmulovich, K.I., Fedkin, V.V., 1987. The H_2O and CO_2 regime in regional metamorphism. International Geology Review 29, 1379-1401.

Aranovich, L.Y., Dubinina, E.O., Avdeenko, A.S., Lebedeva, Y.M., Bushmin, S.A.,

649 Dolivo-Dobrovol'skii, D.D., 2010. Oxygen isotopic composition of coexisting minerals of
650 sillimanite-hypersthene rocks from the Por'ya bay area: Evidence of fluid involvement in
651 granulite-facies metamorphism. Geochemistry International 48, 739-751.

652 Aranovich, L.Y., Newton, R.C., Manning, C.E., 2013. Brine-assisted anatexis: Experimental melting
653 in the system haplogranite–H_2O–NaCl–KCl at deep-crustal conditions. Earth and Planetary
654 Science Letters 374, 111-120.

655 Asami, M., Shiraishi, K., 1987. Kyanite from the western part of the Sør Rondane Mountains, East
656 Antarctica. Proceedings of the NIPR symposium on Antarctic Geosciences 1, 150-168.

657 Asami, M., Osanai, Y., Shiraishi, K., Makimoto, H., 1992. Metamorphic evolution of the Sør Rondane
658 Mountains, East Antarctica. In: Yoshida, Y., Kaminuma, K., Shiraishi, K. (Eds.), Recent
659 Progress in Antarctic Earth Science. Terra Scientific Publishing Company, Tokyo, pp. 7–15.

660 Baba, S., Osanai, Y., Nakano, N., Owada, M., Hokada, T., Horie, K., Adachi, T., Toyoshima, T., 2013.
661 Counterclockwise P–T path and isobaric cooling of metapelites from Brattnipene, Sør Rondane
662 Mountains, East Antarctica: Implications for a tectonothermal event at the proto-Gondwana
663 margin. Precambrian Research 234, 210–228.

664 Brown, M., 2013. Granite: From genesis to emplacement. GSA Bulletin 125, 1079–1113.

665 Dubinina E.O., Aranovich, L.Y., van Reenen, D.D., Avdeenko, A.S., Varlamov, D.A., Shaposhnikov,
666 V.V., Kurdyukov, E.B., 2015. Involvement of fluids in the metamorphic processes within

667 different zones of the Southern Marginal Zone of the Limpopo complex, South Africa: An
668 oxygen isotope perspective. Precambrian Research 256, 48-61.
669 Elburg, M.A., Andersen, T., Jacobs, J., Läufer, A., Ruppel, A., Krohne, N., Damaske, D., 2016. One
670 Hundred Fifty Million Years of Intrusive Activity in the Sør Rondane Mountains (East
671 Antarctica): Implications for Gondwana Assembly. The Journal of Geology 124, 1-26.
672 Glassley, W.E., Korstgårda, J.A., Sørensen, K., 2010. K-rich brine and chemical modification of the
673 crust during continent–continent collision, Nagssugtoqidian Orogen, West Greenland.
674 Precambrian Research 180, 47–62.
675 Goldoff, B., Webster, J.D., Harlov, D.E., 2012. Characterization of fluor-chlorapatites by electron
676 probe microanalysis with a focus on time-dependent intensity variation of halogens. American
677 Mineralogist 97, 1103-1115.
678 Grantham, G.H., Macey, P.H., Ingram, B.A., Roberts, M.P. Armstrong, R.A., Hokada, T., Shiraishi,
679 K., Jackson, C., Bisnath A., Manhica V., 2008. Terrane correlation between Antarctica,
680 Mozambique and Sri Lanka; comparisons of geochronology, lithology, structure and
681 metamorphism and possible implications for the geology of southern Africa and
682 Antarctica..Geological Society, London, Special Publications 308, 91-119.
683 Grantham, G.H., Macey, P.H., Horie, K., Kawakami, T., Ishikawa, M., Satish-Kumar, M., Tsuchiya,
684 N., Graser, P., Azevedo, S., 2013. Comparison of the metamorphic history of the Monapo

685 Complex, northern Mozambique and Balchenfjella and Austhameren areas Sør Rondane,
686 Antarctica: Implications for the Kuunga Orogeny and the amalgamation of N and S.
687 Gondwana. Precambrian Research 234, 85–135.

688 Grew, E.S., Asami, M., Makimoto, H., 1989. Preliminary petrological studies of the metamorphic
689 rocks of the eastern Sør Rondane Mountains. Proceedings of the NIPR symposium on Antarctic
690 Geosciences 3, 100-127.

691 Harlov, D.E., Förster, H.J., 2002. High-grade fluid metasomatism on both a local and a regional scale:
692 the Seward Peninsula, Alaska, and the Val Strona di Omegna, Ivrea-Verbano Zone, northern
693 Italy. Part 1: Petrography and silicate mineral chemistry. Journal of Petrology 43, 769-799.

694 Heinrich, W., 2007. Fluid immiscibility in metamorphic rocks. Fluid-fluid interactions. Reviews in
695 Mineralogy and Geochemistry 65, 389-430.

696 Higashino, F., Kawakami, T., Satish-Kumar, M., Ishikawa, M., Maki, K., Tsuchiya, N., Grantham,
697 G.H., Hirata, T., 2013a. Chlorine-rich fluid or melt activity during granulite facies
698 metamorphism in the Late Proterozoic to Cambrian continental collision zone- An example
699 from the Sør Rondane Mountains, East Antarctica. Precambrian Research 234, 229-246.

700 Higashino, F., Kawakami, T., Satish-Kumar, M., Ishikawa, M., Tsuchiya, N., Grantham, G.H., 2013b.
701 Multi-stage Cl-rich fluid activity and behavior of REE-bearing minerals in a Neoproterozoic
702 granulite terrane. Goldschmidt 2013 abstract, Mineralogical Magazine 77, 1298.

703 Higashino, F., Kawakami, T., Tsuchiya, N., Satish-Kumar, M., Ishikawa, M., Grantham, G.H., Sakata,
704 S., Hattori, K., Hirata, T., 2015a. Geochemical behavior of zirconium during Cl-rich aqueous
705 fluid infiltration under upper amphibolite facies metamorphism – A case study from
706 Brattnipene, Sør Rondane Mountains, East Antarctica. Journal of Mineralogical and
707 Petrological Sciences 110, 166-178.
708 Higashino, F., Kawakami, T., Tsuchiya, N., Satish-Kumar, M., Ishikawa, M., Grantham, G.H., 2015b.
709 Mass transfer in mafic gneiss during upper-amphibolite facies chloride brine infiltration.
710 Goldschmidt 2015 abstract, 1268.
711 Hiroi Y., Yanagi A., Kato M., Kobayashi T., Prame B., Hokada T., Satish-Kumar M., Ishikawa M.,
712 Adachi, T., Osanai Y., Motoyoshi Y., Shiraishi GK., 2014. Supercooled melt inclusions in
713 lower-crustal granulites as a consequence of rapid exhumation by channel flow. Gondwana
714 Research 25, 226–234.
715 Holdaway, M.J., 2000. Application of new experimental and garnet Margules data to the garnet–
716 biotite geothermometer. American Mineralogist 85, 881–892.
717 Holdaway, M.J., 2001. Recalibration of the GASP geobarometer in light of recent garnet and
718 plagioclase activity models and versions of the garnet-biotite geothermometer. American
719 Mineralogist 86, 1117-1129.
720 Holdaway, M.J., Mukhopadhyay, B., Dyar, M.D., Guidotti, C.V., Dutrow, B.L., 1997. Garnet-biotite

721 geothermometry revised: New Margules parameters and a natural specimen data set from
722 Maine. American Mineralogist 82, 582-595.

723 Holness, M.B., 1997. Surface chemical controls on pore-fluid connectivity in texturally equilibrated
724 materials. In: Jamtveit, B., Yardley, B.W.D. (Eds.), Fluid Flow and Transport in Rocks.
725 Chapman and Hall, London, pp. 149–169.

726 Holness, M.B., Cesare, B., Sawyer, E.W., 2011. Melted rocks under the microscope: Microstructures
727 and their interpretation. Elements 7, 247–252.

728 Ishikawa, M., Kawakami, T., Satish-Kumar, M., Grantham, G.H., Hokazono, Y., Saso, M., Tsuchiya,
729 N., 2013. Late Neoproterozoic extensional detachment in eastern Sør Rondane Mountains, East
730 Antarctica: Implications for the collapse of East African Antarctic Orogen. Precambrian
731 Research 234, 247-256.

732 Icenhower, J., London, D., 1997. Partitioning of fluorine and chlorine between biotite and granitic
733 melt: experimental calibration at 200 MPa H_2O. Contributions to Mineralogy and Petrology
734 127, 17-29.

735 Jacobs, J., Bauer, W., Fanning, C.M., 2003. Late Neoproterozoic/Early Palaeozoic events in central
736 Dronning Maud Land and significance for the southern extension of the East African Orogen
737 into East Antarctica. Precambrian Research 126, 27-53.

738 Jacobs, J., Elburg, M., Läufer, A., Kleinhanns, I.C., Henjes-Kunst, F., Estrada, S., Ruppel, A.S.,

739 Damaske, D., Montero, P., Bea, F., 2015. Two distinct Late Mesoproterozoic/Early
740 Neoproterozoic basement provinces in central/eastern Dronning Maud Land, East Antarctica:
741 The missing link, 15–21°. Precambrian Research 265, 249-272.
742 Jung, S., Hoernes, S., Mezger, K., 2000. Geochronology and petrology of migmatites from the
743 Proterozoic Damara Belt — importance of episodic fluid-present disequilibrium melting and
744 consequences for granite petrology. Lithos 51, 153–179.
745 Kamei A., Horie K., Owada M., Yuhara M., Nakano N., Osanai Y., Adachi T., Hara Y., Terao M.,
746 Teuchi S., Shimura T., Tsukada K., Hokada T., Iwata C., Shiraishi K., Ishizuka H., Takahashi Y.,
747 2013. Late Proterozoic juvenile arc metatonalite and adakitic intrusions in the Sør Rondane
748 Mountains, Eastern Dronning Maud Land, Antarctica. Precambrian Research 234, 47-62.
749 Kawakami, T., Hokada, T., Sakata, S., Hirata, T., 2016. Possible polymetamorphism indicated by
750 monazite and zircon dating and isotope mapping of garnet, and significance of Cl-rich biotite
751 coexisted with melt in the garnet-sillimanite gneiss, Skallevikshalsen, Lützow-Holm Complex,
752 East Antarctica. Journal of Mineralogical and Petrological Science 111, 129-143.
753 Kawakami, T., Satish-Kumar, M., Tsuchiya, N., Ishikawa, M., Higashino, F., Grantham, G.H.,
754 Yoshida, K., 2010. Pelitic metamorphic rocks from Perlebandet and Balchenfjella, Sør Rondane
755 Mountains, East Antarctica. Abstract of the First Symposium on Polar Science. GO008.
756 Kitano, I., Osanai, Y., Nakano, N., Adachi, T., 2016. Detrital zircon provenances for metamorphic

757 rocks from southern Sør Rondane Mountains, East Antarctica: A new report of Archean to
758 Mesoproterozoic zircons. Journal of Mineralogical and Petrological Science 111, 118-128.
759 Kojima, S., Shiraishi, K., 1986. Note on the geology of the western part of the Sør Rondane
760 Mountains, East Antarctica. Memoirs of National Institute of Polar Research, Special Issue, 43,
761 116-132.
762 Kretz, R., 1983. Symbols for rock-forming minerals. American Mineralogist 68, 277-279.
763 Kullerud, K., 1996. Chlorine-rich amphiboles: interplay between amphibole composition and an
764 evolving fluid. European Journal of Mineralogy 8, 355-370.
765 Kusebauch, C., John, T., Barnes, J.D., Klügel, A., Austrheim, H.O., 2015. Halogen element and stable
766 chlorine isotope fractionation caused by fluid–rock interaction (Bamble Sector, SE Norway).
767 Journal of Petrology 56, 299-324.
768 Li, Z., Tainosho, Y., Shiraishi, K., Owada, M., 2003. Chemical characteristics of fluorine-bearing
769 biotite of early Paleozoic plutonic rocks from the Sør Rondane Mountains, East Antarctica.
770 Geochemical Journal 37, 145–161.
771 Li, Z., Du, Z., Yang, S., Chen, H., Song, B., Liu, D., 2006. First report of zircon SHRIMP U–Pb dating
772 from the Dufek granite in the Sør Rondane Mountains, East Antarctica. Journal of Zhejiang
773 University Science A (Suppl. II), 315–319.
774 Li, Z.L., Chen, H., Yang, S., Tainosho, Y., Shiraishi, K., Owada, M., 2007. Fluid components in

775 accessory minerals of Pan-African granitoids in the Sør Rondane Mountains, East Antarctica.
776 Journal of Zhejiang University Science A 8, 1004-1010.
777 Ludwig, K.R., 2012. User's manual for Isoplot 3.75. A geological toolkit for Microsoft Excel.
778 Berkeley Geochronology Center Special Publication No.5 (revision of January 30, 2012. 75
779 pp.).
780 Manning, C.E., Aranovich, L.Y., 2014. Brines at high pressure and temperature: Thermodynamic,
781 petrologic and geochemical effects. Precambrian Research 253, 6-16.
782 Markl, G., Bucher, K., 1998. Composition of fluids in the lower crust inferred from metamorphic salt
783 in lower crustal rocks. Nature 391, 781-783.
784 Mathez, E.A., Webster, J.D., 2005. Partitioning behavior of chlorine and fluorine in the system
785 apatite-melt-fluid. Geochimica et Cosmochimica Acta 69, 1275-1286.
786 Meert, J., 2003. A synopsis of events related to the assembly of eastern Gondwana. Tectonophysics
787 362, 1–40.
788 Mieth, M., Jacobs, J., Ruppel, A., Damaske, D., Läufer, A., Jokat, W., 2014. New detailed
789 aeromagnetic and geological data of eastern Dronning Maud Land: Implications for refining the
790 tectonic and structural framework of Sør Rondane, East Antarctica. Precambrian Research 245,
791 174-185.
792 Milord, I., Sawyer, E.W., Brown, M., 2001. Formation of diatexite migmatite and granite magma

793 during anatexis of semi-pelitic metasedimentary rocks: an example from St. Malo, France.
794 Journal of Petrology 42, 487-505.

795 Munoz, J.L., Swenson, A., 1981. Chrolide-hydroxyl exchange in biotite and estimation of relative
796 HCl/HF activities in hydrothermal fluids. Economic Geology 76, 2212-2221.

797 Munoz, J.L., 1992. Calculation of HF and HCl fugacities from biotite compositions: revised equations.
798 Geological Society of America, Abstract with Programs 24, A221.

799 Newton, R.C., Aranovich,L.Y., Hansen,E.C., Vandenheuvel,B.A., 1998. Hypersaline fluids in
800 Precambrian deep-crustal metamorphism. Precambrian Research 91, 41-63.

801 Newton, R.C., Touret, J.L.R., Aranovich, L.Y., 2014. Fluids and H_2O activity at the onset of granulite
802 facies metamorphism. Precambrian Research 253, 17-25.

803 Osanai, Y., Shiraishi, K., Takahashi, Y., Ishizuka, H., Tainosho, Y., Tsuchiya, N., Sakiyama, T.,
804 Kodama, S., 1992. Geochemical characteristics of metamorphic rocks from the central Sør
805 Rondane Mountains, East Antarctica. In: Yoshida, Y., Kaminuma, K., Shiraishi, K. (Eds.),
806 Recent Progress in Antarctic Earth Science. Terra Scientific Publishing Company, Tokyo, pp.
807 17–27.

808 Osanai, Y., Nogi, Y., Baba, S., Nakano, N., Adachi, T., Hokada, T., Toyoshima, T., Owada, M.,
809 Satish-Kumar, M., Kamei, A., Kitano, I., 2013. Geologic evolution of the Sør Rondane
810 Mountains, East Antarctica: Collision tectonics proposed based on metamorphic processes and

811 magnetic anomalies. Precambrian Research 234, 8-29.

812 Otsuji, N., Satish-Kumar, M., Kamei, A., Tsuchiya, N., Kawakami, T., Ishikawa, M., Grantham, G. H.,
813 2013. Late-Tonian to early-Cryogenian apparent depositional ages for metacarbonate rocks
814 from the Sør Rondane Mountains, East Antarctica. Precambrian Research 234, 257-278.

815 Otsuji, N., Satish-Kumar, M., Kamei, A., Takazawa, E., Tsuchiya, N., Grantham, G. H., Kawakami, T.,
816 Ishikawa, M., Osanai, Y., 2016. Sr and Nd Isotopic evidence in metacarbonate rocks for an
817 extinct Island arc - ocean system in East Antarctica. Journal of Mineralogical and Petrological
818 Sciences 111, 170-180.

819 Piccoli, P., Candela, P., 1994. Apatite in felsic rocks: a model for the estimation of initial halogen
820 concentrations in the Bishop Tuff (Long Valley) and Tuolumne intrusive suite (Sierra Nevada
821 Batholith) magmas. American Journal of Science 294, 92-135.

822 Rubatto, D., 2002. Zircon trace element geochemistry: partitioning with garnet and the link between
823 U–Pb ages and metamorphism. Chemical Geology 184, 123-138.

824 Rubenach, M.J., 2005. Relative timing of albitization and chlorine enrichment in biotite in Proterozoic
825 schists, Snake Creek anticline, Mount Isa inlier, Northeastern Australia. The Canadian
826 Mineralogist 43, 349-366.

827 Ruppel, A.S., Läufer, A., Jacobs, J., Elburg, M., Krohne, N., Damaske, D., Lisker, F., 2015. The Main
828 Shear Zone in Sør Rondane, East Antarctica: Implications for the late-Pan-African tectonic

829 evolution of Dronning Maud Land. Tectonics 34, 1290-1305.

830 Safonov, O.G., Kosova, S.A., Van Reenen, D.D., 2014. Interaction of biotite-amphibole gneiss with
831 H_2O-CO_2-(K, Na)Cl fluids at 550MPa and 750 and 800ºC: Experimental study and applications
832 to dehydration and partial melting in the middle crust. Journal of Petrology 55, 2419-2456.

833 Selby, D., Nesbitt, B.E., 2000. Chemical composition of biotite from the Casino porphyry Cu-Au-Mo
834 mineralization, Yukon, Canada: evaluation of magmatic and hydrothermal fluid chemistry.
835 Chemical Geology 171, 77-93.

836 Shiraishi, K., Kojima, S., 1987. Basic and intermediate gneisses from the western part of the Sør
837 Rondane Mountains, East Antarctica. Proceedings of the NIPR symposium on Antarctic
838 Geosciences 1, 129-149.

839 Shiraishi, K., Asami, M., Ishizuka, H., Kojima, H., Kojima, S., Osanai, Y., Sakiyama, T., Takahashi,
840 Y., Yamazaki, M., Yoshikura, S., 1991. Geology and metamorphism of the Sør Rondane
841 Mountains, East Antarctica. In: Thomson, M.R.A., Crame, J.A., Thomson, J.W. (Eds.),
842 Geological Evolution of Antarctica. Cambridge University Press, Cambridge, pp. 77–82.

843 Shiraishi, K., Osanai, Y., Tainosho, Y., Takahashi, Y., Tsuchiya, N., Kojima, S., Yanai, K., Moriwaki,
844 K., 1992. Geological map of Widerøefjellet. Antarctic Geological Map Series, sheet 32, scale
845 1:100,000, National Institute of Polar Research, Tokyo.

846 Shiraishi, K., Osanai, Y., Ishizuka, H., Asami, M., 1997. Geological map of the Sør Rondane

847 Mountains, Antarctica. Antarctic Geological Map Series, sheet 35, scale 1:250,000, National
848 Institute of Polar Research, Tokyo.

849 Shiraishi, K., Dunkley, D.J., Hokada, T., Fanning, C.M., Kagami, H., Hamamoto, T., 2008.
850 Geochronological constrains on the Late Proterozoic to Cambrian crustal evolution of eastern
851 Dronning Maud Land, East Antarctica: a synthesis of SHRIMP U-Pb age and Nd model age
852 data. Geological Society of London, Special Publications 308, 21–67.

853 Spear, F.S., Kohn, M.J., Cheney, J.T., 1999. P-T paths from anatectic pelites. Contributions to
854 Mineralogy and Petrology 134, 17-32.

855 Tomkins, H.S., Powell, R., Ellis, D.J., 2007. The pressure dependence of the zirconium-in-rutile
856 thermometer. Journal of metamorphic Geology 25, 703-713.

857 Touret, J.L.R., Huizenga, J.M., 2011. Fluids in granulites. The Geological Society of America Memoir
858 207, 25-37.

859 Touret, J.L.R., Santosh, M., Huizenga, J.M., 2016. High-temperature granulites and supercontinents.
860 Geoscience Frontiers 7, 101-113.

861 Toyoshima, T., Osanai, Y., Baba, S., Hokada, T., Nakano, N., Adachi, T., Otsubo, M., Ishikawa, M.,
862 Nogi, Y., 2013. Sinistral transpressional and extensional tectonics in Dronning Maud Land,
863 East Antarctica, including the Sør Rondane Mountains. Precambrian Research 234, 30-46.

864 Tsuchiya, N., Ishikawa, M., Satish-Kumar, M., Kawakami, T., Kojima, H., Kaiden, H., Miura, H.,

865 Suganuma, Y., Abe, M., Sasaki, D., Chiba, M., Okada, Y., Hashizume, F., Grantham, G.,
866 Goderis, S., 2012. Report on geological fieldwork in the Sør Rondane Mountains, Eastern
867 Dronning Maud Land, 2009–2010 (JARE-51). Antarctic Record 56, 295–379.
868 Van den Berg, R., Huizenga, J.M., 2001. Fluids in granulites of the Southern Marginal Zone of the
869 Limpopo Belt, South Africa. Contributions to Mineralogy and Petrology 141, 529-545.
870 Watson, E.B., Brenan, J.M., 1987. Fluids in lithosphere, 1. Experimentally determined wetting
871 characteristics of CO_2-H_2O fluids and their implications for fluid transport, host-rock physical
872 properties and fluid inclusion formation. Earth and Planetary Science Letters 85, 594–615.
873 Webster, J.D., 1992. Fluid-melt interactions involving Cl-rich granites: Experimental study from 2 to 8
874 kbar. Geochimica et Cosmochimica Acta 56, 659-678.
875 Weinberg, R.F., Hasalová, P., 2015. Water-fluxed melting of the continental crust: A review. Lithos
876 212-215, 158-188.
877 Wu, C.-M., Zhang, J., Ren, L.-D., 2004. Empirical garnet-biotite-plagioclase-quartz (GBPQ)
878 geobarometry in medium- to high-grade metapelites. Journal of Petrology 45, 1907-1921.
879 Yardley, B.W.D., Barber, J.P., 1991. Melting reactions in the Connemara Schists: the role of water
880 infiltration in the formation of amphibolite facies migmatites. American Mineralogist 76, 848–
881 856.
882 Zack, T., Moraes, A.R., Kronz, A.A., 2004. Temperature dependence of Zr in rutile: empirical

883 calibration of a rutile thermometer. Contributions to Mineralogy and Petrology 148, 471-488.

884 Zhu, C., Sverjensky, D.A., 1991. Partitioning of F-Cl-OH between minerals and hydrothermal fluids.

885 Geochimica et Cosmochimica Acta 55, 1837-1858.

886 Zhu, C., Sverjensky, D.A., 1992. F-Cl-OH partitioning between biotite and apatite. Geochimica et

887 Cosmochimica Acta 56, 3435-3467.

888

889 **Figure captions**

890 Figure 1. (a) Gondwana amalgamation model by Neoproterozoic orogens. East African Orogen and

891 Kuunga Orogen (Meert, 2003) are shown. Position of the Sør Rondane Mountains is shown by

892 a star. (b) Geological map of the Sør Rondane Mountains, East Antarctica (modified after

893 Shiraishi et al., 1997, 2008; Osanai et al., 1992; 2013; Toyoshima et al., 2013; Ishikawa et al.,

894 2013), showing the location of Perlebandet. Chlorine concentrations of biotite (circles) and

895 amphibole (squares) in pelitic and mafic gneisses (Higashino et al., 2013a; 2015a) are also

896 shown. Warm color represents biotite or hornblende with higher-Cl contents. Note that Cl-rich

897 biotite and hornblende are localized near tectonic boundaries and shear zones. location 4;

898 location 4 of Higashino et al. (2013). The Main Tectonic Boundary (O) is after Osanai et al.

899 (2013) and the Main Tectonic Boundary (M) is after Mieth et al. (2014). (c) Geological map of

900 Perlebandet after Shiraishi et al. (1992). Sample localities are also shown.

Figure 2. (a) Garnet porphyroblast including abundant sillimanite needles in the core. Sillimanite is also arranged along the gneissose structure of the matrix (top). Sample 2602D. Plane polarized light (PPL). (b)-(o) Mode of occurrence of metamorphic minerals in a garnet-sillimanite-biotite gneiss (sample 3001G). (b) Sillimanite including Zn-bearing spinel overgrown by garnet. This microstructure is interpreted to represent staurolite breakdown. Crossed polarized light (CPL). (c) Sillimanite porphyroblast with the inclusion-poor core and inclusion-rich rim. Subgrain boundaries can be clearly observed. CPL. (d) Enlargement of the dotted square in (c). Zn-bearing spinel is included in the inclusion-rich rim of the sillimanite porphyroblast. Cl-rich biotite and ilmenite are included in the inclusion-poor core of the sillimanite. PPL. (e) Sillimanite, andalusite and biotite replacing garnet. PPL. (f) Garnet rim replaced by biotite + andalusite intergrowth with minor fibrolitic sillimanite. PPL. (g) BSE image of breakdown microstructure of garnet replaced by biotite, plagioclase, andalusite + quartz intergrowth, kyanite and muscovite. Outlines of kyanite grains are indicated by red lines. (h) Panchromatic CL image of the same area as (g). Warm colors indicate higher CL intensity. Note the high CL intensity of kyanite compared to low CL intensity of andalusite. (i) BSE image of breakdown microstructure of garnet replaced by biotite, plagioclase, quartz, andalusite, kyanite and sillimanite. Sillimanite includes Zn-bearing spinel grains. Outline of kyanite grains are indicated by red lines. (j) Panchromatic CL image of the same area as (i).

919 Warm colors indicate higher CL intensity. Note the high CL intensity of kyanite compared to
920 moderate and low intensity of sillimanite and andalusite, respectively. (k) Garnet including
921 sillimanite and Zn-bearing spinel, which is partly replaced by the aggregate of Bt + And + Sil +
922 Crn + Spl + Ms at the rim. PPL. (l) CPL of (k). Sillimanite is separately included in garnet,
923 whereas andalusite and sillimanite are found in the replacement microstructure of garnet. (m)
924 Garnet that is including Zn-bearing spinel is partly replaced by the retrograde aggregate of Bt +
925 And + Ky + Sil + Spl. PPL. (n) CPL of (m). Note that andalusite and kyanite (right), as well as
926 andalusite and sillimanite (center) are in direct contact. (o) A BSE image of rutile partly
927 replaced by ilmenite. Both of them are included in garnet.

928 Figure 3. Plots showing the variations of biotite composition depending on the mode of occurrence. (a)
929 TiO_2 (wt.%) vs X_{Mg} plot for sample 3001G. (b) Cl (wt.%) vs X_{Mg} plot for sample 3001G. (c)
930 TiO_2 (wt.%) vs X_{Mg} plot for sample 3001B. (d) Cl (wt.%) vs X_{Mg} plot for sample 3001B. (e)
931 TiO_2 (wt.%) vs X_{Mg} plot for sample 2601C. (b) Cl (wt.%) vs X_{Mg} plot for sample 2601C.

932 Figure 4. X-ray elemental mappings and BSE images showing the mode of occurrence of Cl-rich
933 biotite from samples 3001B (a-c) and 2601C (d-f). (a) BSI of garnet including Cl-rich biotite
934 and apatite. Garnet is partly replaced by retrograde biotite at the rim and along the cracks. (b)
935 X-ray elemental map of Cl for the area including (a). Cl-rich biotite (yellow to yellowish green)
936 is present as inclusions in garnet and as a matrix phase (especially at the top of the map).

937 Retrograde biotite replacing garnet has lower Cl content (light blue). Apatite included in garnet
938 is enriched in Cl. (c) X-ray elemental map of Mg for the same area as (b). Some of the Cl-rich
939 biotite grains included in garnet show higher Mg content (red) than the matrix biotite (greenish
940 yellow). (d) BSI of garnet partly replaced by biotite-plagioclase intergrowths. (e) X-ray
941 elemental maps of Cl for the area including (d). Cl-rich biotite is present as an isolate matrix
942 phase (yellowish green). Moderately Cl-bearing biotite is present as a biotite-plagioclase
943 intergrowth replacing garnet (light blue). (f) X-ray elemental map of Mg for the same area as
944 (d).

945 Figure 5. CL images of zircon from Perlebandet. (a)-(h) Sample 3001G. (i)-(l) Sample 3001B. (m)-(t)
946 Sample 2601C. Red circles represent the pits of the LA-ICPMS U-Pb dating (5 μm) and
947 numbers given are the $^{206}Pb/^{238}U$ age ± 2S.D. error [better than 95-105% concordance, where
948 concordance = ($^{206}Pb/^{238}U$ age)*100/($^{207}Pb/^{235}U$ age)] and Th/U ratio. *in Grt bd*; zircon present
949 in garnet breakdown microstructure developed around garnet. *matrix*; zircon present in the
950 matrix. *in Grt/Sil rim*; zircon included in garnet/sillimanite rim. *** Ma; discordant data point.

951 Figure 6. (a)-(c) Concordia diagrams and probability density plot (inset) for the LA-ICPMS U-Pb
952 zircon dating. Concordant data (concordance = 95-105%) are used to construct the probability
953 density plot. Color variation of the error ellipses represents Th/U ratio of the dated spots. Note
954 that ages older than ca. 1200 Ma is absent in all samples. (a) Sample 3001G. (b) Sample 3001B.

(c) Sample 2601C. (d) A plot showing the relationship between concordant age vs Th/U ratio of the analyzed spots.

Figure 7. Pressure-temperature diagram showing a *P-T-t* path (red arrows) for Perlebandet rocks. Evolution of microstructure for sample 3001G is given as sketches (1)-(3) and change of fluid compositions along the *P-T-t* path is also indicated. Note that Cl-rich fluid is present from prograde metamorphism. Petrogenetic grid for the NaKFMASH system with contours of Mg/(Fe+Mg) = 0.1-0.4 in garnet in divariant Als + Grt + Bt assemblage are from Spear et al. (1999). Prograde, peak and retrograde *P-T* estimates by the Grt-Bt geothermometer (GB) (Holdaway et al., 1997; Holdaway, 2000) and the GASP geobarometer (Holdaway, 2001) are shown as gray, red and black squares, respectively. Peak *P-T* estimate by the Zr-in-rutile geothermometer (Tomkins et al., 2007), the Grt-Bt geothermometer (Holdaway et al., 1997; Holdaway, 2000) and the GASP geobarometer (Holdaway, 2001) is shown by a red broken diamond. Zr-in-rutile$_{1550}$ represents a result of the Zr-in-rutile geothermometer (Tomkins et al., 2007) for 1550 ppm Zr, and Zr-in-rutile$_{2200}$ represents that for 2200 ppm Zr. Retrograde *P-T* estimates by the Grt-Bt geothermometer (Holdaway et al., 1997; Holdaway, 2000) and the GBPQ geobarometer (Wu et al., 2004) using compositions of garnet rims and biotite and plagioclase in the biotite-plagioclase intergrowths are shown as solid squares, where green, blue and brown squares are from samples 3001B, 3001G and 2601C, respectively. These

973 estimates would accompany errors of ±50 °C and ±0.1 GPa, which are not shown for
974 simplicity. Numbers of the reactions correspond to those in the text. Reactions (4)-(6) are not
975 shown.

976 Figure 8. Simplified cross section showing the tectonic model for the continental collision in the SRM,
977 modified after Osanai et al. (2013). Chlorine-rich fluid infiltration in Perlebandet presumably
978 took place at the uppermost part of the footwall of the MBT. Chlorine-rich fluid infiltration in
979 Balchenfjella is dated to be at ca. 603 Ma (Higashino et al., 2013), and would be an older event
980 than that in Perlebandet (ca. 580 Ma). BDF: Balchen Detachment Fault (Ishikawa et al., 2013).
981 *1 This study, *2 Higashino et al. (2015a), *3 Higashino et al. (2013).

982 Table 1. Representative mineral analysis of biotite, garnet and plagioclase from samples 3001G,
983 3001B and 2601C. The log[$f(H_2O)/f(HCl)$] and log[$f(H_2O)/f(HF)$] values of the fluid that
984 possibly coexisted with Cl-bearing biotite (Munoz, 1992) are also shown. *1 Based on Munoz
985 (1992). *2 Temperature used in calculating log[$f(H_2O)/f(HCl)$] and log[$f(H_2O)/f(HF)$] values of
986 the fluid possibly coexisted with biotite. Temperature was estimated using the Grt-Bt
987 geothermometer (Holdaway et al., 1997; Holdaway, 2000) and the GASP (Holdaway, 2001)
988 and Grt-Bt-Pl-Qtz (Wu et al., 2004) geobarometers. *3 Temperature was estimated using
989 Zr-in-rutile geothermometer by Tomkins et al. (2006) and GASP geobarometer (Holdaway,
990 2001).

991 Supplementary Table 2. Summary of the results of LA-ICPMS U-Pb zircon dating.

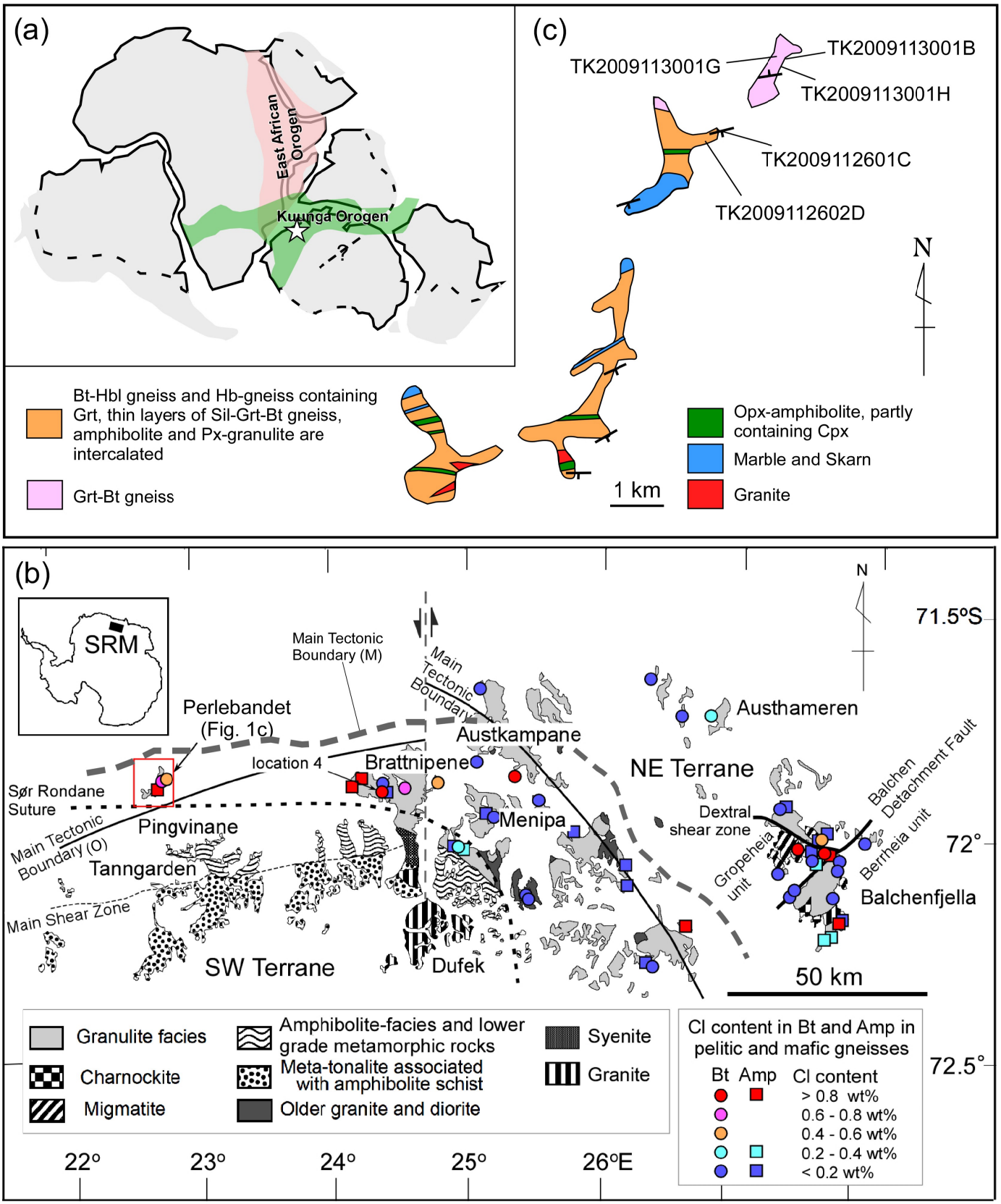

Kawakami et al. Fig. 1

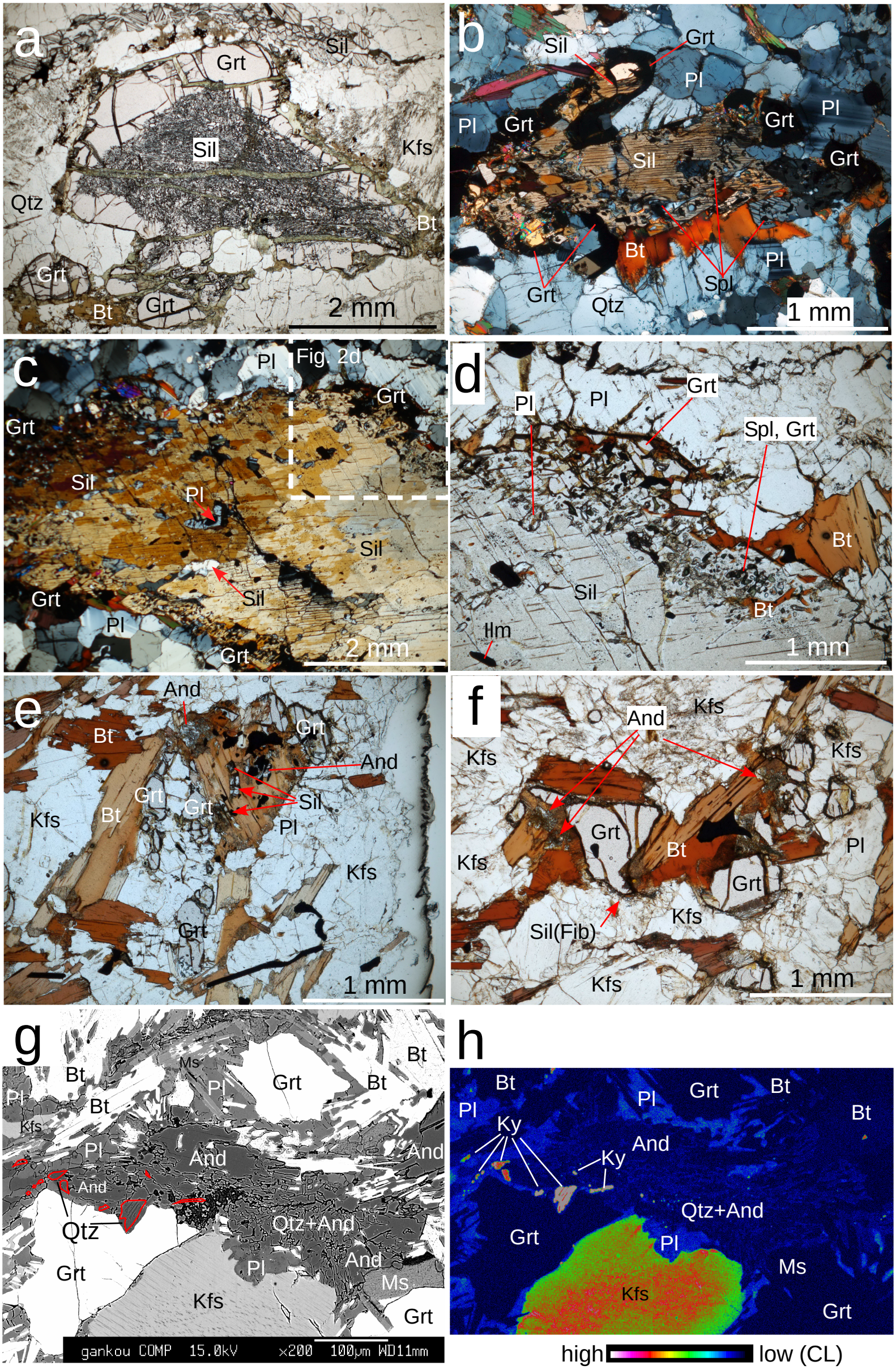

Kawakami et al. Fig. 2

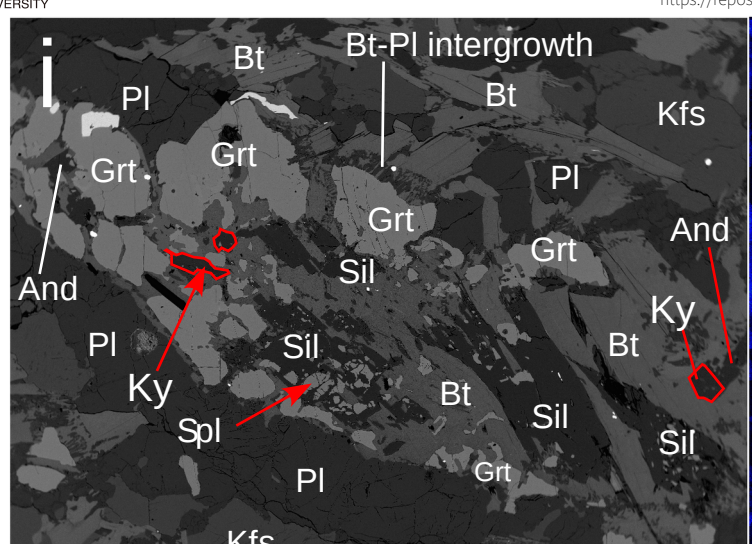

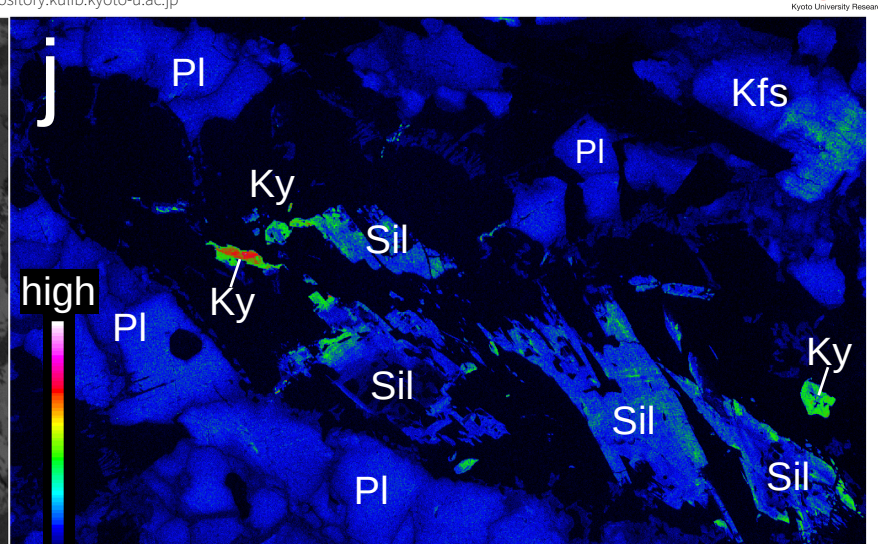

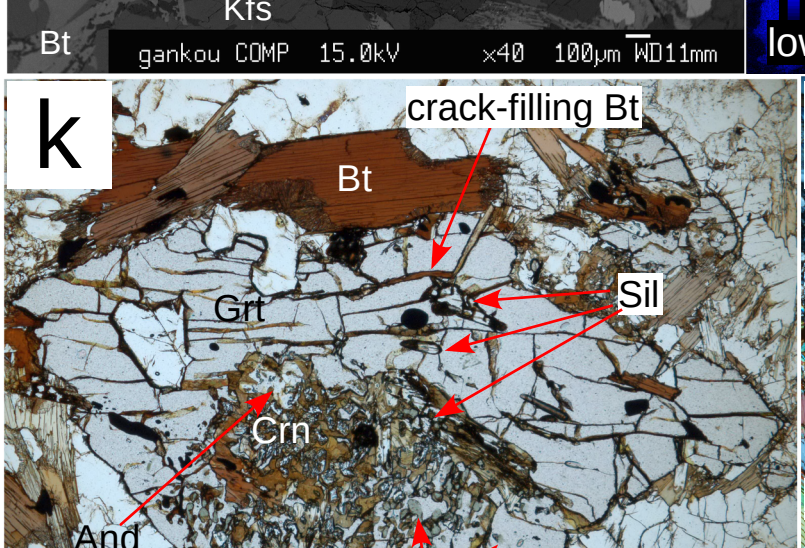

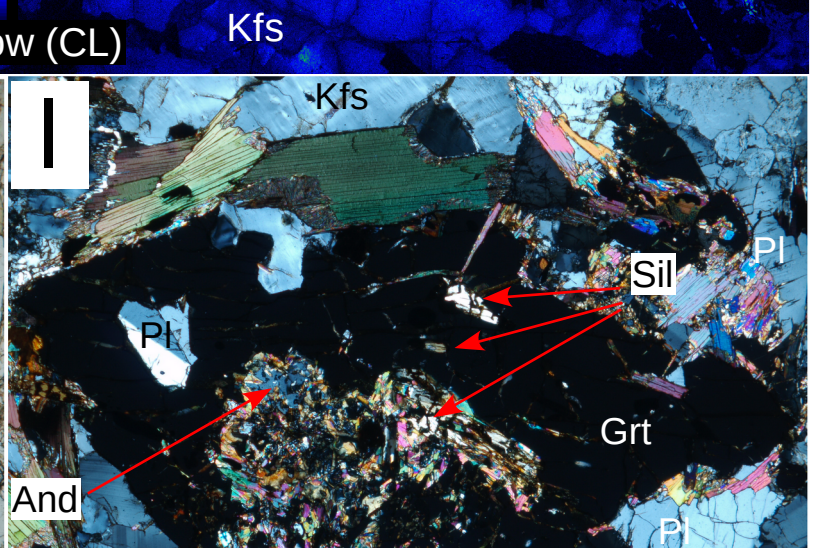

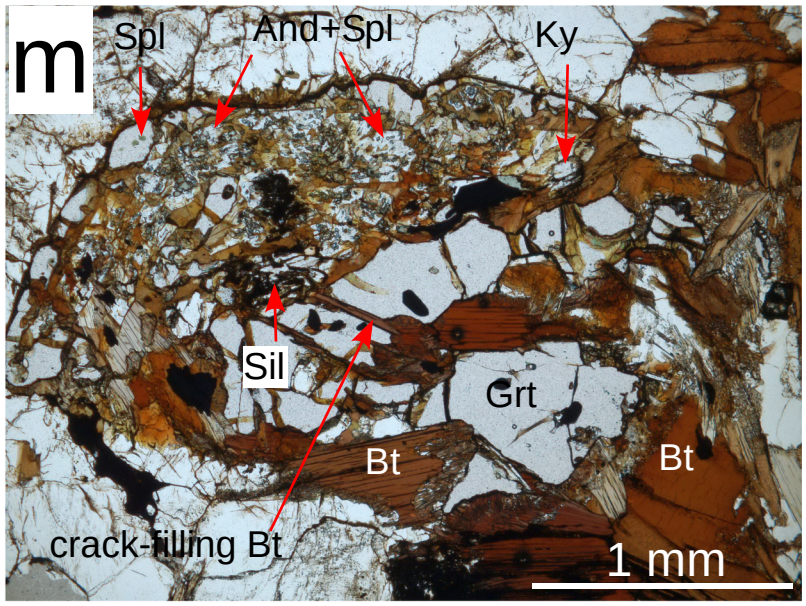

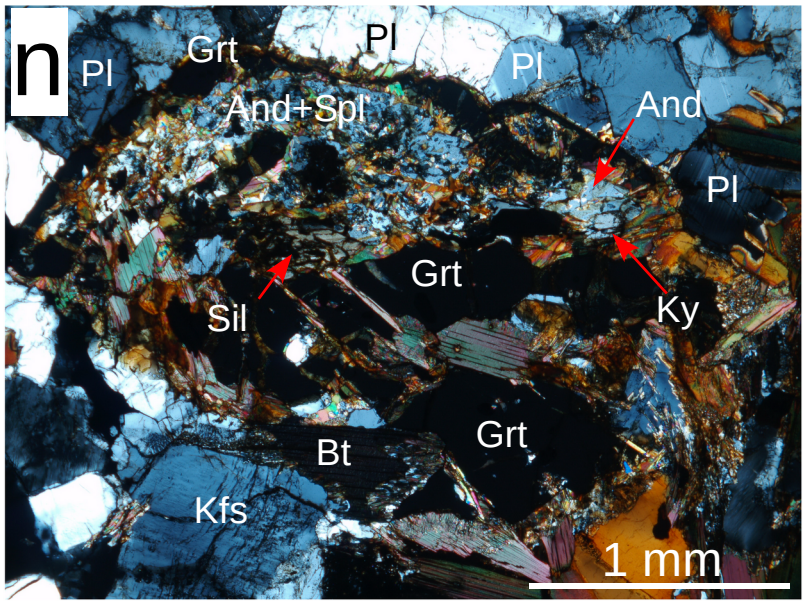

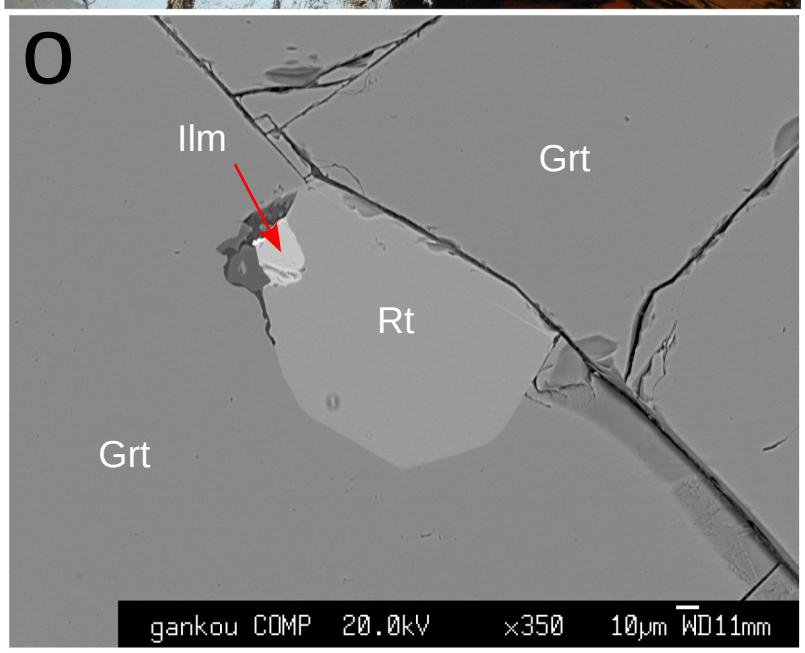

Kawakami et al Fig 2 (continued)

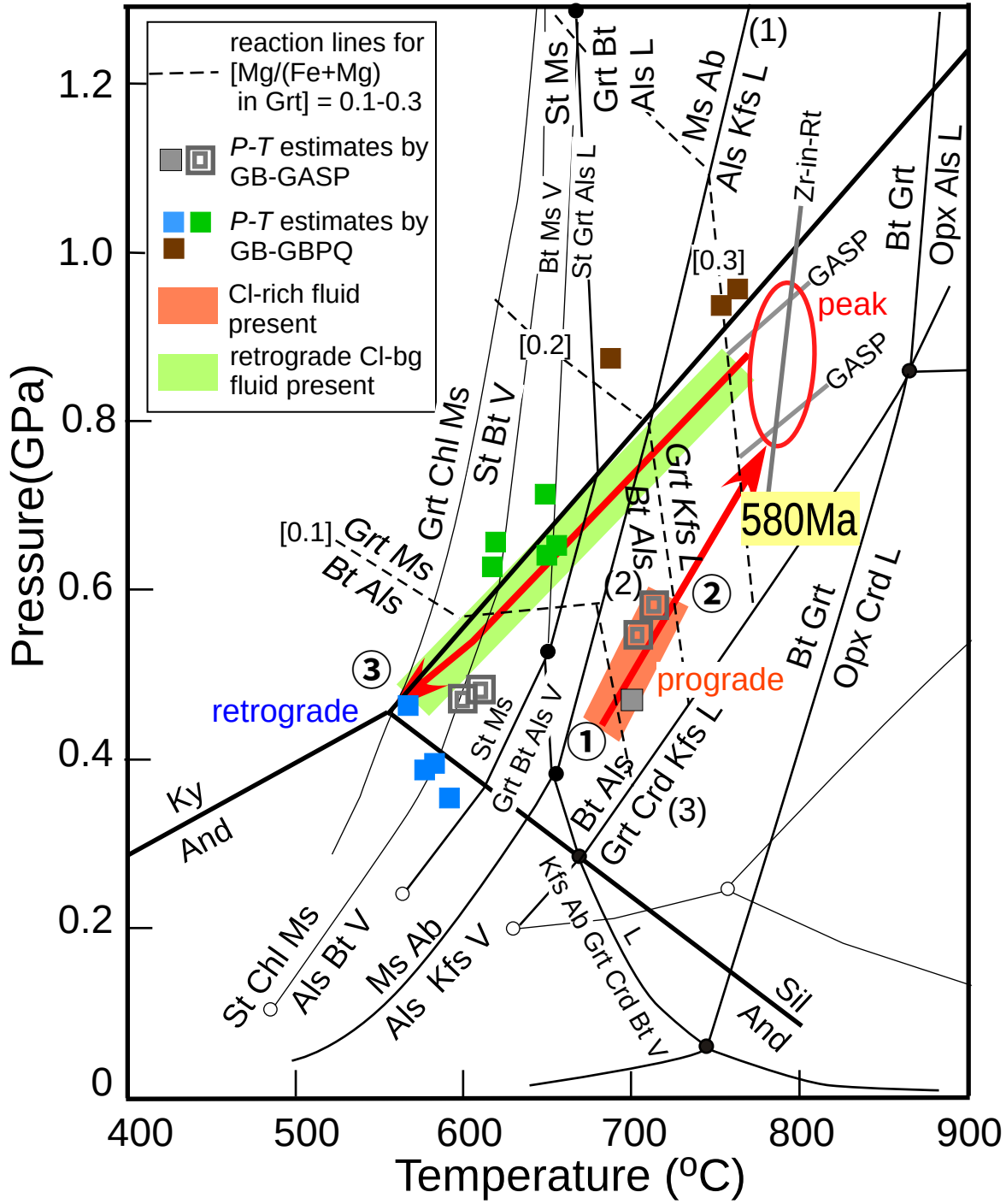

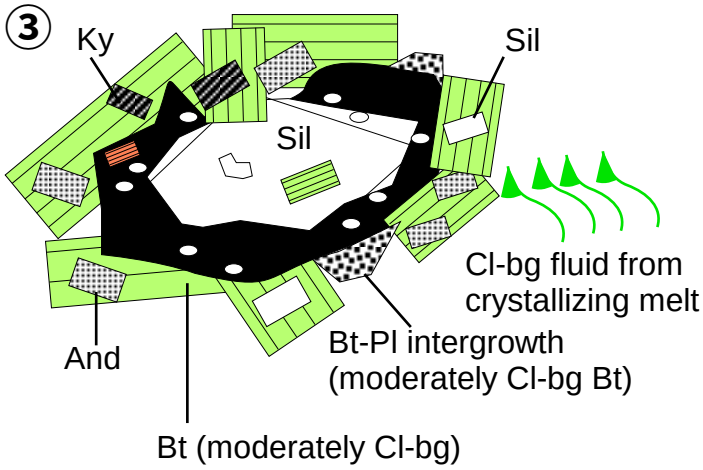

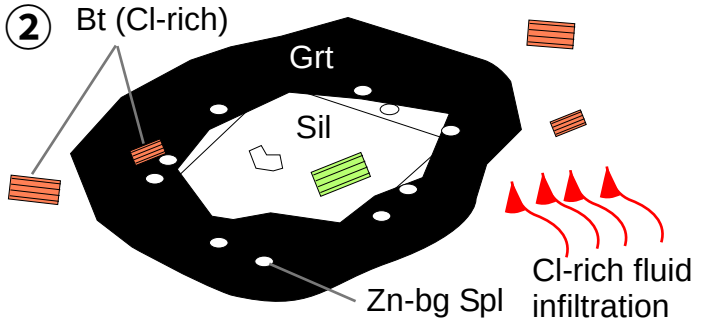

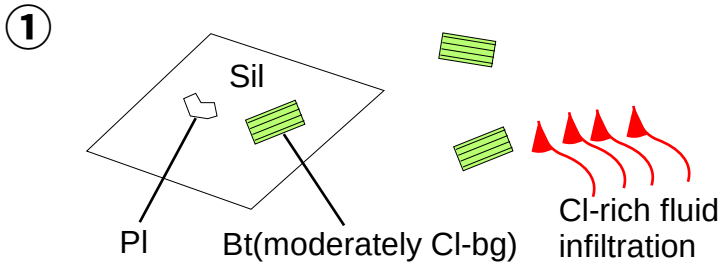

Kawakami et al. Fig 7

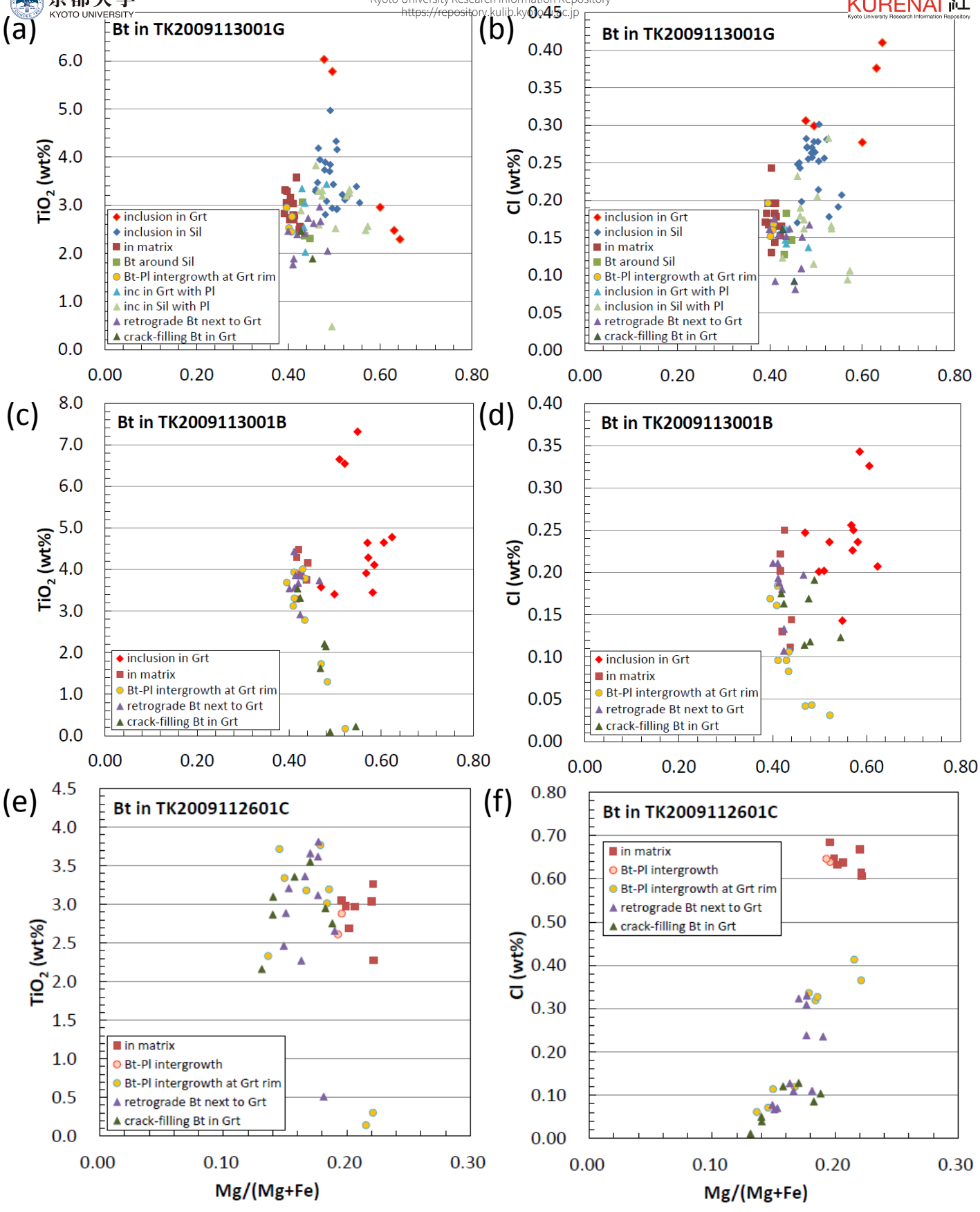

Kawakami et al. Fig. 3

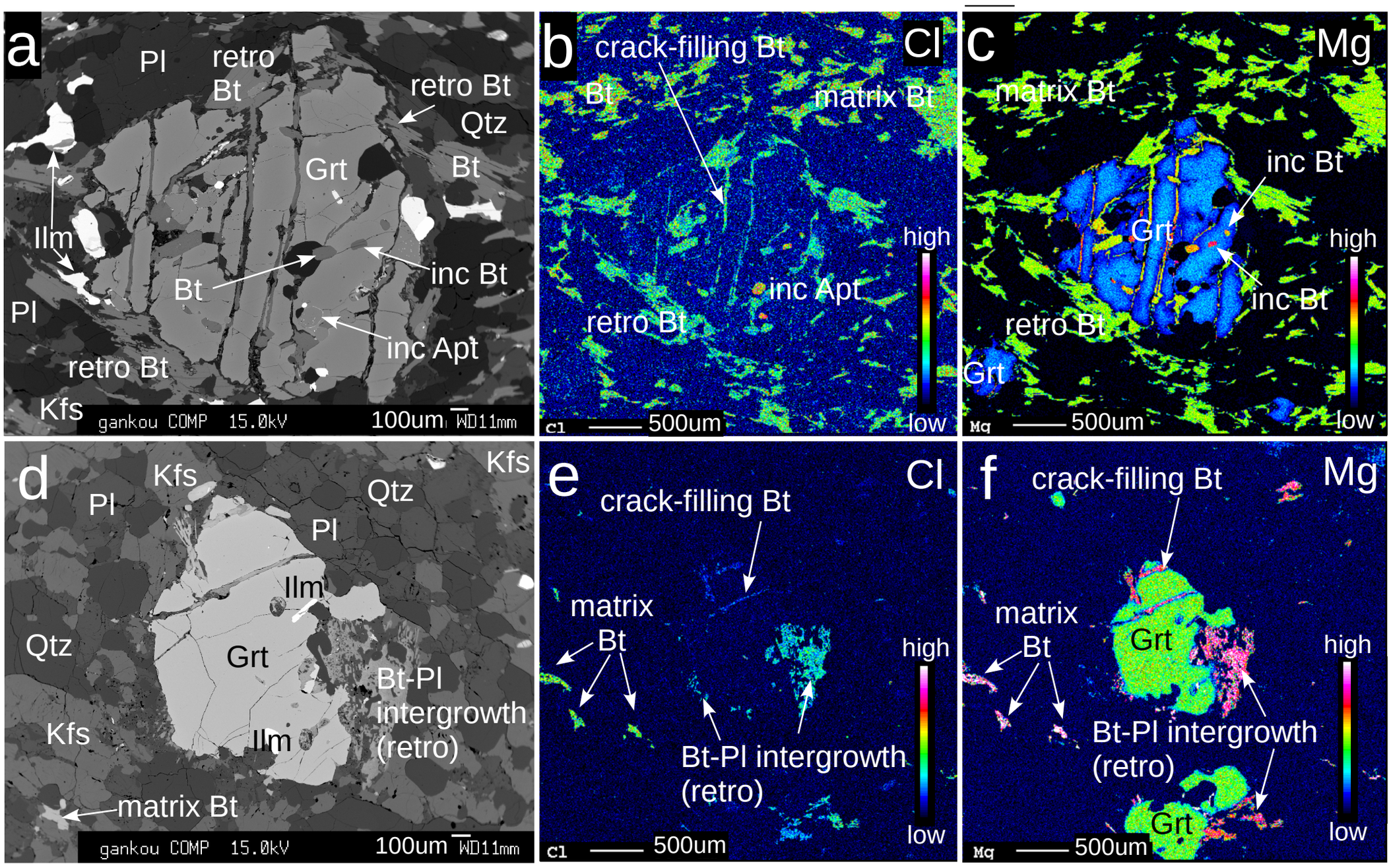

Kawakami et al Fig 4

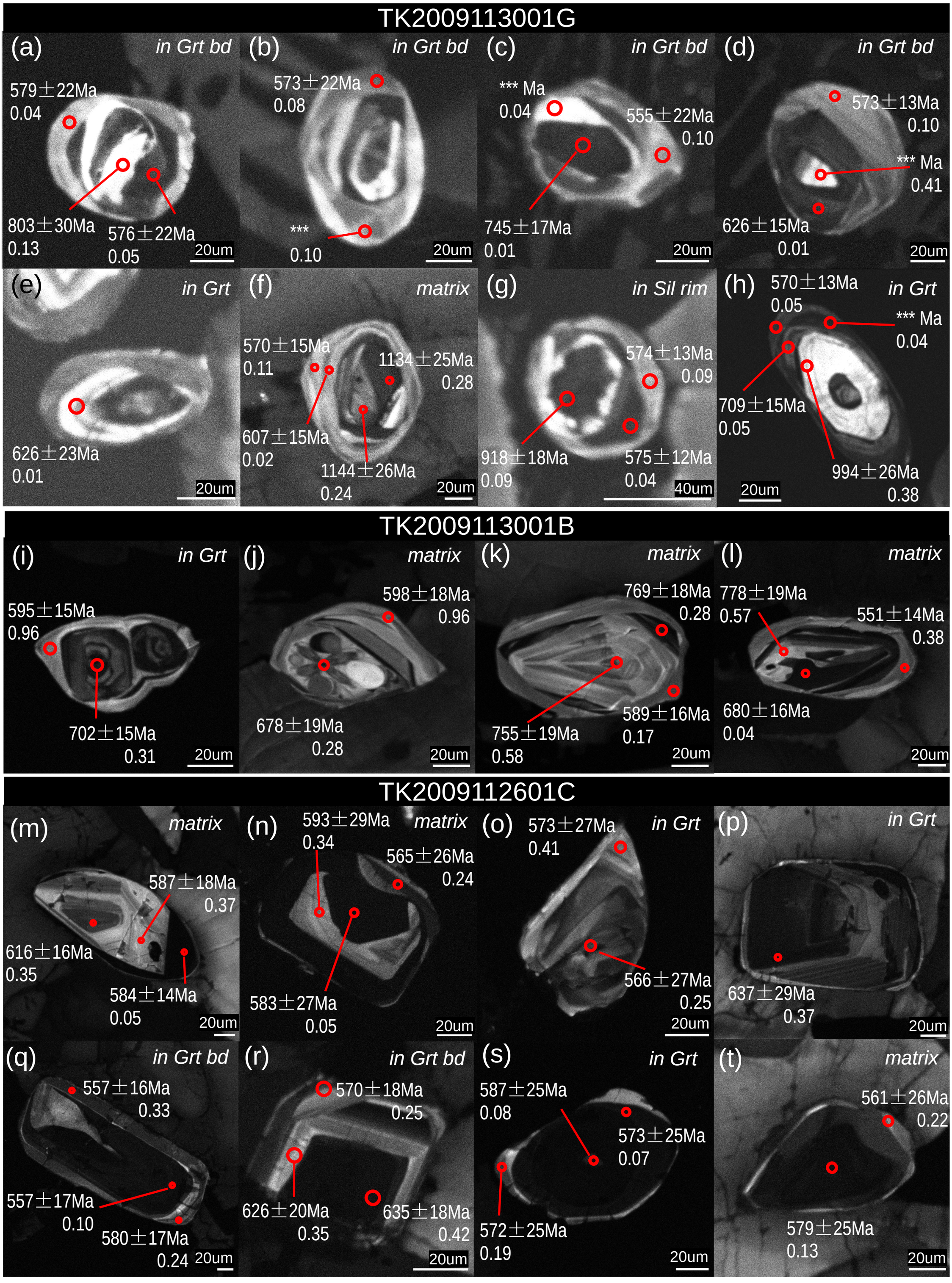

Fig. 5 Kawakami et al.

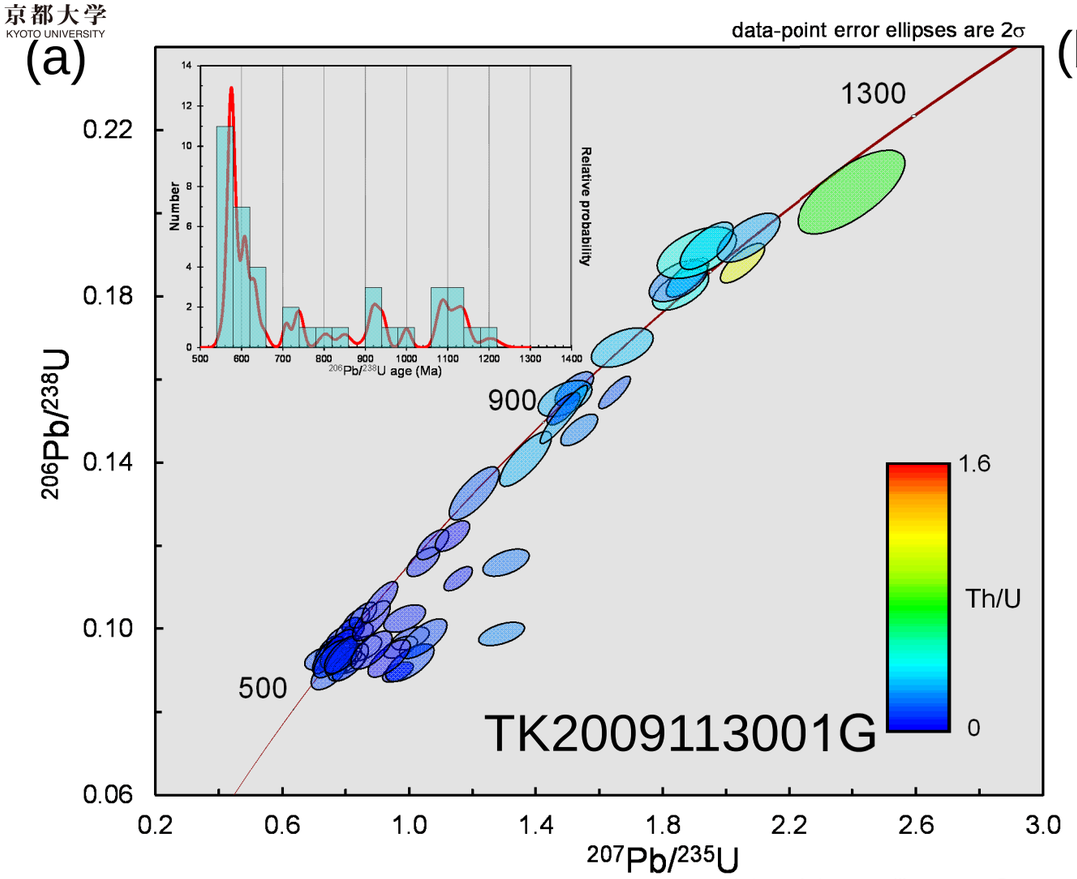

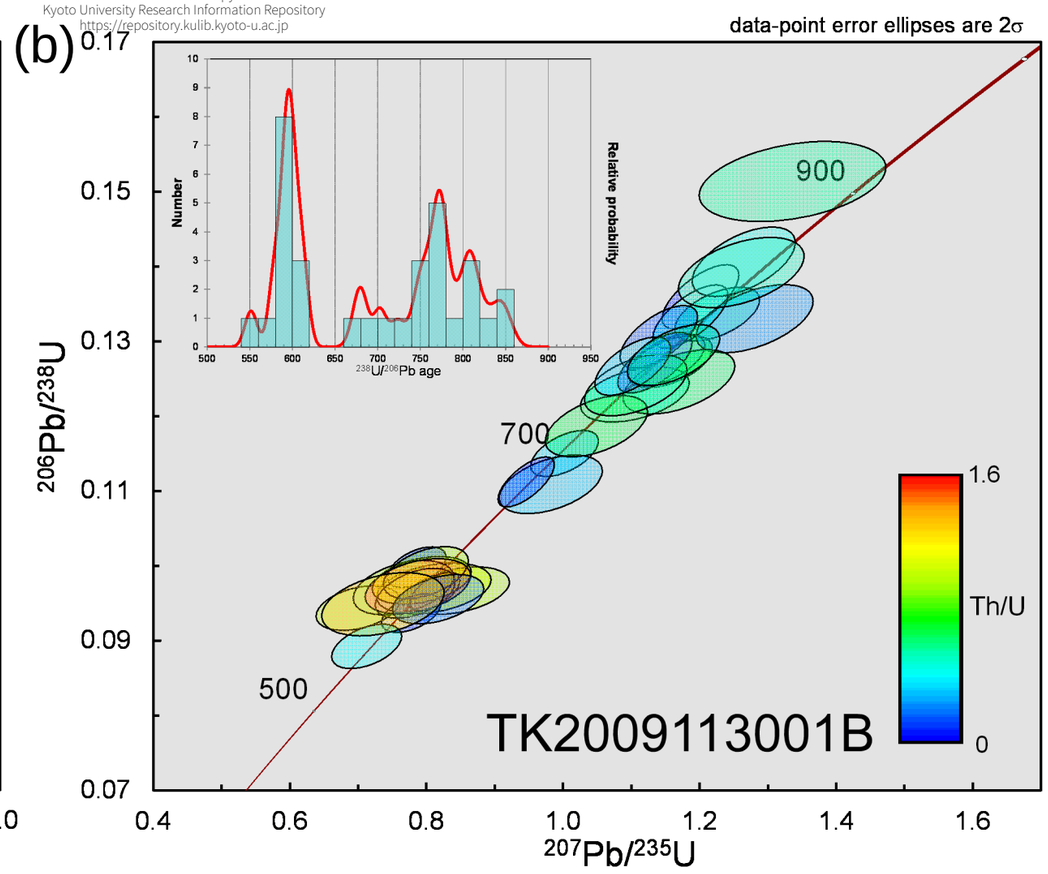

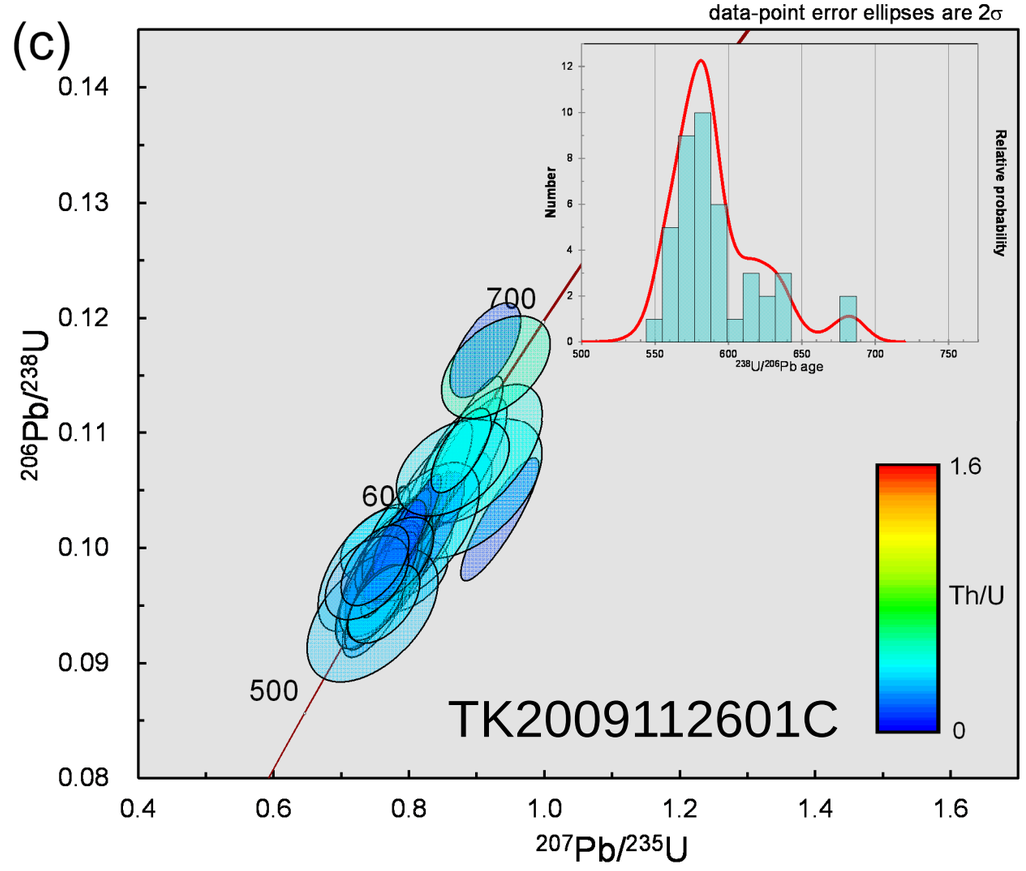

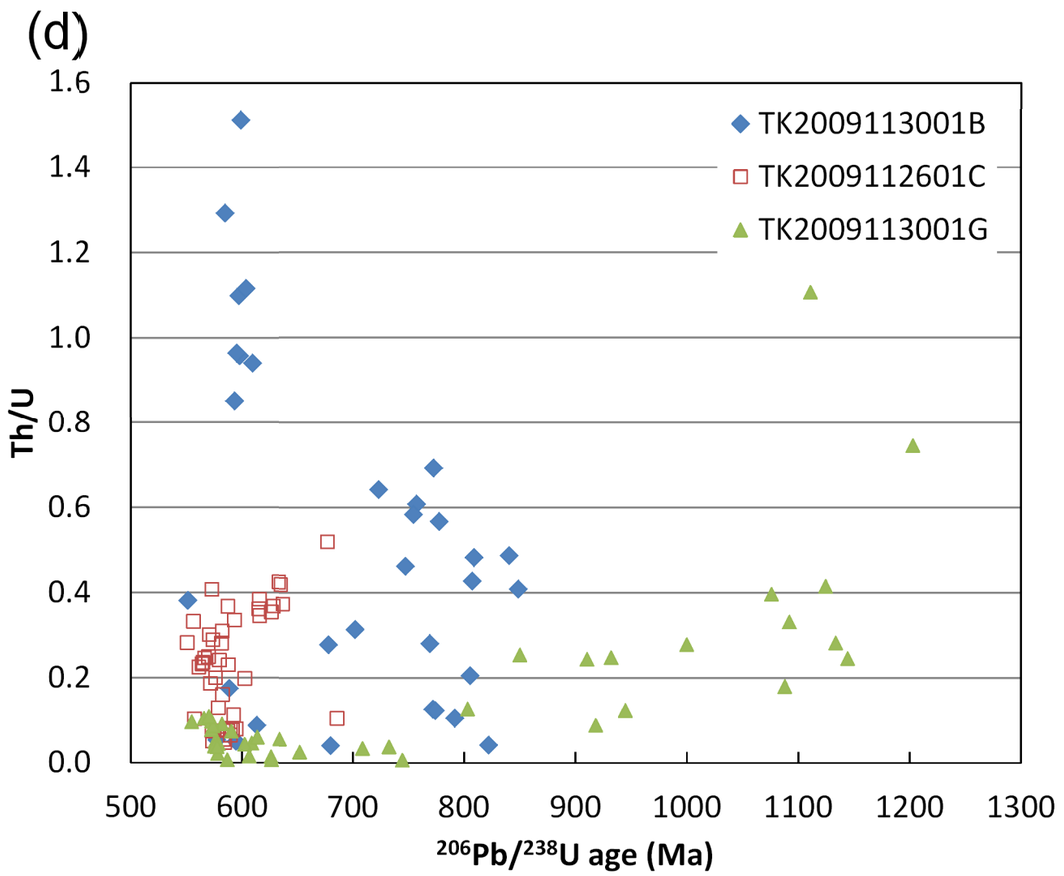

Kawakami et al. Fig. 6

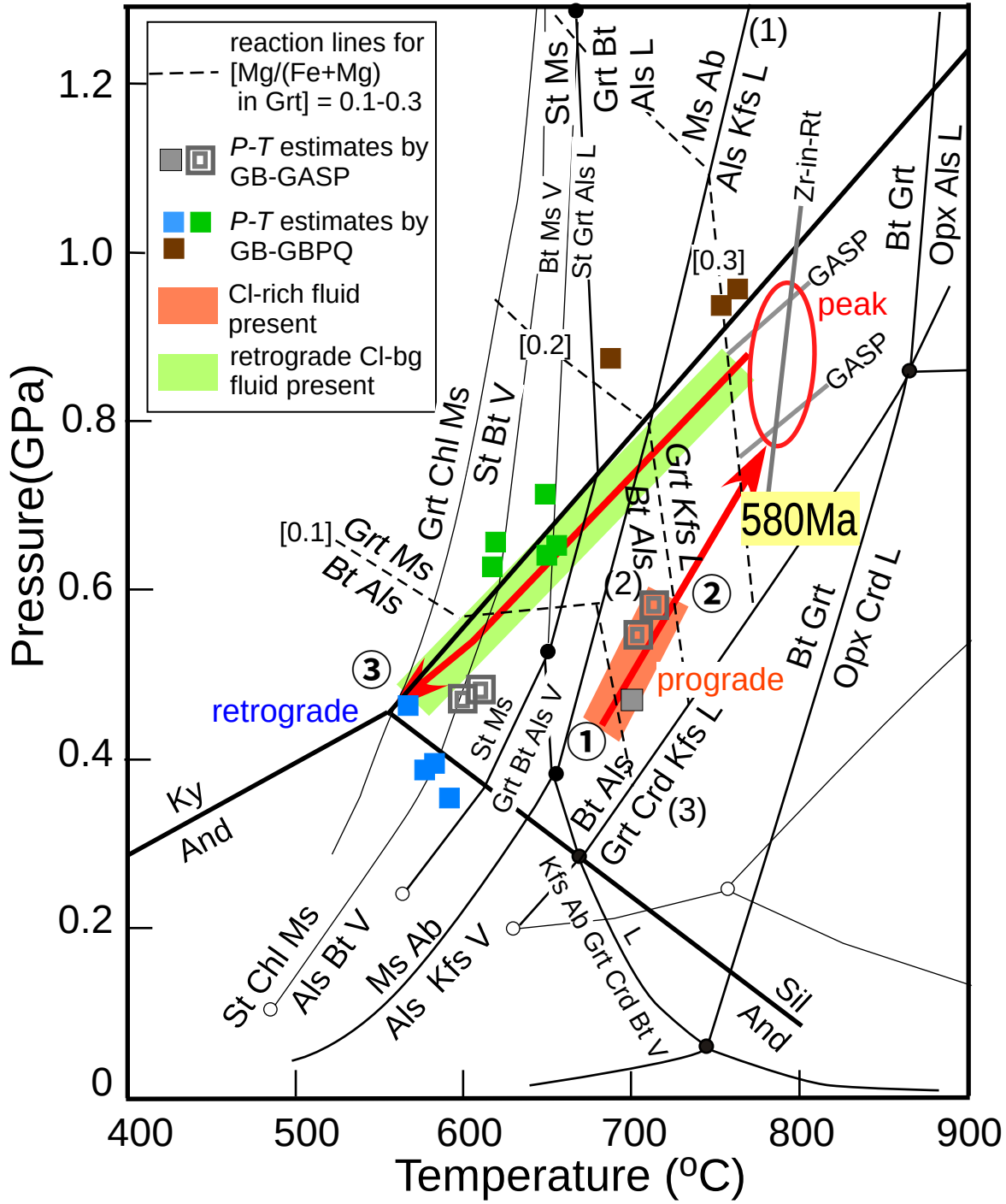

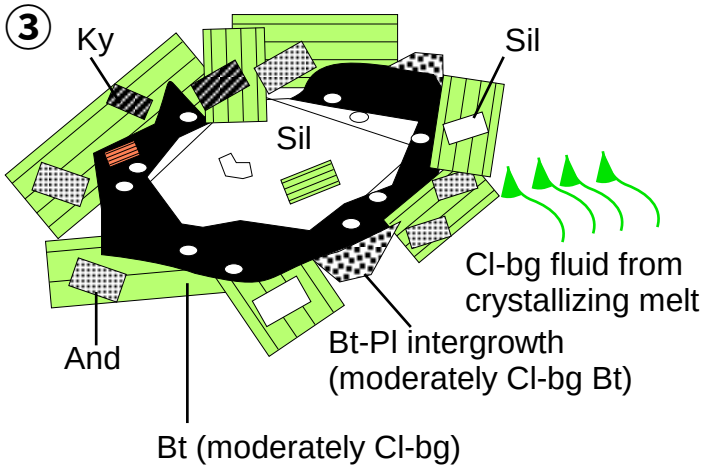

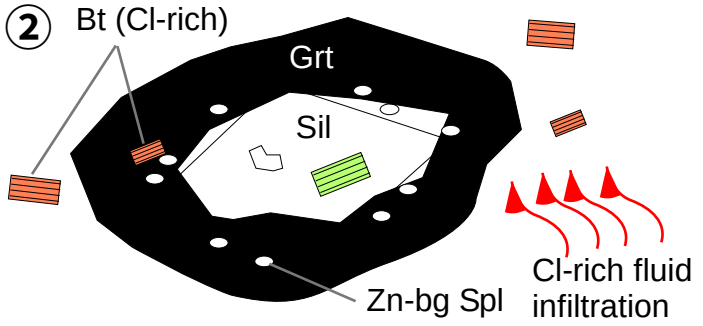

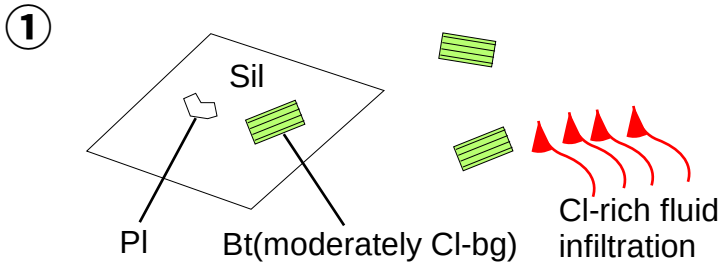

Kawakami et al. Fig 7

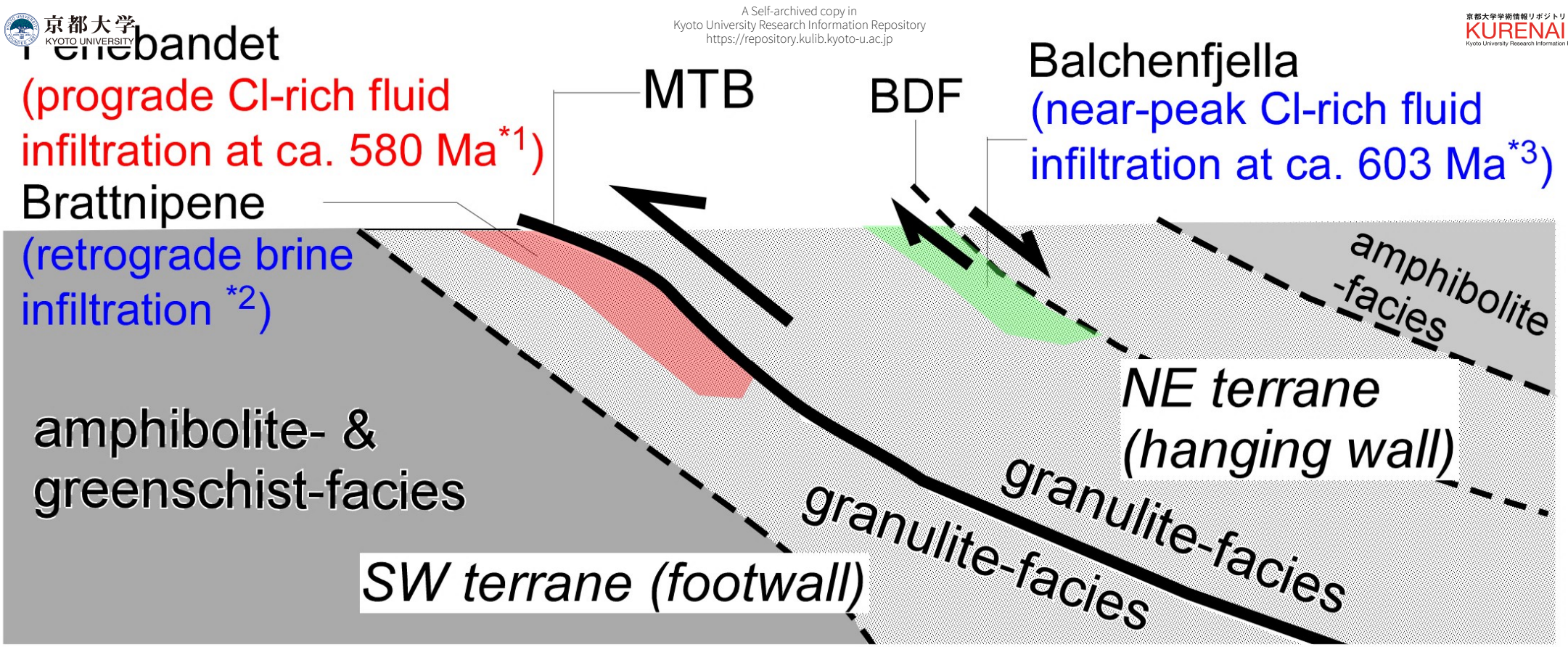

Fig. 8 Kawakami et al.

sample	TK2009113001G																TK2009112601C				
mineral	Pl	Pl	Pl	Pl	Grt	Grt	Grt	Grt	Spl	Bt	Bt	Bt	Bt	Bt	Bt	Bt	Grt	Grt	Pl	Pl	Pl
occurrence	inclusion in Sil	inclusion in Sil	Pl moat around Sil (Sil side)	Pl moat around Sil (Kfs side)	overgrowth on Sil	overgrowth on Sil	in matrix	in matrix	inclusion in Sil rim	inclusion in Grt	inclusion in Sil	in matrix (isolated)	in matrix (isolated)	Bt-Pl intergrowth replacing Grt	retrograde Bt next to Grt	crack-filling Bt in Grt	in matrix	in matrix	in matrix	in matrix	Bt-Pl intergrowth replacing Grt
core/rim	core	rim			core	rim	core	rim									rim	core	rim	core	
SiO_2	59.65	59.71	61.01	62.14	38.95	37.76	37.81	37.48	0.14	37.70	34.78	36.68	35.85	35.29	34.92	35.44	38.00	38.33	61.41	61.19	61.89
TiO_2	0.00	0.06	0.00	0.10	0.00	0.02	0.05	0.00	0.00	2.29	4.19	3.15	3.58	2.76	2.39	1.89	0.01	0.08	0.01	0.00	0.03
Al_2O_3	26.02	25.63	24.76	23.72	22.00	21.18	21.72	21.26	61.03	19.12	18.50	18.91	19.30	19.04	18.94	20.28	21.23	21.10	23.93	24.06	23.88
Cr_2O_3	0.00	0.00	0.00	0.00	0.02	0.08	0.00	0.06	0.11	0.00	0.06	0.10	0.05	0.07	0.09	0.01	0.00	0.04	0.00	0.00	0.00
FeO	0.11	0.05	0.00	0.02	32.31	36.58	35.68	36.04	27.07	13.57	19.09	20.20	20.43	20.39	21.17	18.59	33.74	31.81	0.06	0.02	0.38
ZnO	n.d.	n.d.	n.d.	n.d.	n.d.	n.d.	n.d.	n.d.	6.03	n.d.	n.d.	n.d.	n.d.	n.d.	n.d.	n.d.	n.d.	n.d.	n.d.	n.d.	n.d.
MnO	0.01	0.00	0.02	0.00	0.62	1.44	0.84	1.83	0.06	0.11	0.04	0.02	0.06	0.04	0.14	0.05	0.77	0.82	0.03	0.00	0.02
MgO	0.00	0.00	0.00	0.00	4.90	2.38	3.26	2.48	5.56	13.74	9.33	7.68	8.21	7.89	7.90	8.64	1.48	1.95	0.01	0.00	0.02
CaO	7.78	6.92	6.54	5.52	2.29	1.49	2.27	1.44	0.00	0.08	0.02	0.00	0.00	0.01	0.00	0.00	6.36	7.17	5.90	5.94	5.60
BaO	0.15	0.06	0.09	0.02	0.11	0.06	0.11	0.00	0.00	0.06	0.30	0.08	0.16	0.05	0.00	0.00	0.09	0.00	0.02	0.00	0.00
Na_2O	7.24	7.65	7.95	8.69	0.00	0.02	0.04	0.02	0.00	0.19	0.05	0.12	0.10	0.11	0.12	0.16	0.07	0.00	8.14	8.20	8.35
K_2O	0.23	0.19	0.25	0.16	0.02	0.01	0.00	0.00	0.04	9.13	9.58	9.63	9.56	10.01	9.77	9.87	0.01	0.03	0.28	0.15	0.15
F	n.d.	n.d.	n.d.	n.d.	n.d.	n.d.	n.d.	n.d.	n.d.	0.36	0.08	0.06	0.09	0.16	0.07	0.16	n.d.	n.d.	n.d.	n.d.	n.d.
Cl	n.d.	n.d.	n.d.	n.d.	n.d.	n.d.	n.d.	n.d.	n.d.	0.41	0.24	0.24	0.17	0.17	0.15	0.09	n.d.	n.d.	n.d.	n.d.	n.d.
-O≡F	n.d.	n.d.	n.d.	n.d.	n.d.	n.d.	n.d.	n.d.	n.d.	0.15	0.03	0.03	0.04	0.07	0.03	0.07	n.d.	n.d.	n.d.	n.d.	n.d.
-O≡Cl	n.d.	n.d.	n.d.	n.d.	n.d.	n.d.	n.d.	n.d.	n.d.	0.09	0.05	0.05	0.04	0.04	0.03	0.02	n.d.	n.d.	n.d.	n.d.	n.d.
Total	101.18	100.26	100.62	100.37	101.22	101.03	101.78	100.61	100.04	96.51	96.16	96.80	97.48	95.87	95.60	95.09	101.76	101.32	99.78	99.56	100.31
number of O	8	8	8	8	12	12	12	12	4	22	22	22	22	22	22	22	12	12	8	8	8
Si	2.64	2.66	2.70	2.75	3.03	3.02	2.98	3.01	0.00	5.50	5.28	5.52	5.37	5.40	5.37	5.40	3.01	3.03	2.73	2.73	2.74
Ti	0.00	0.00	0.00	0.00	0.00	0.00	0.00	0.00	0.00	0.25	0.48	0.36	0.40	0.32	0.28	0.22	0.00	0.00	0.00	0.00	0.00
Al	1.36	1.34	1.29	1.24	2.02	2.00	2.02	2.01	2.00	3.29	3.31	3.35	3.41	3.43	3.43	3.64	1.98	1.96	1.26	1.27	1.25
Cr	0.00	0.00	0.00	0.00	0.00	0.00	0.00	0.00	0.00	0.00	0.01	0.01	0.01	0.01	0.01	0.00	0.00	0.00	0.00	0.00	0.00
Fe	0.00	0.00	0.00	0.00	2.10	2.45	2.36	2.42	0.63	1.66	2.42	2.54	2.56	2.61	2.72	2.37	2.23	2.10	0.00	0.00	0.01
Mn	0.00	0.00	0.00	0.00	0.04	0.10	0.06	0.12	0.00	0.01	0.00	0.00	0.01	0.00	0.02	0.01	0.05	0.05	0.00	0.00	0.00
Mg	0.00	0.00	0.00	0.00	0.57	0.28	0.38	0.30	0.23	2.99	2.11	1.72	1.83	1.80	1.81	1.96	0.17	0.23	0.00	0.00	0.00
Ca	0.37	0.33	0.31	0.26	0.19	0.13	0.19	0.12	0.00	0.01	0.00	0.00	0.00	0.00	0.00	0.00	0.54	0.61	0.28	0.28	0.27
Ba	0.00	0.00	0.00	0.00	0.00	0.00	0.00	0.00	0.00	0.00	0.02	0.00	0.01	0.00	0.00	0.00	0.00	0.00	0.00	0.00	0.00
Zn	n.d.	n.d.	n.d.	n.d.	n.d.	n.d.	n.d.	n.d.	0.12	n.d.	n.d.	n.d.	n.d.	n.d.	n.d.	n.d.	n.d.	n.d.	n.d.	n.d.	n.d.
Na	0.62	0.66	0.68	0.74	0.00	0.00	0.01	0.00	0.00	0.05	0.02	0.03	0.03	0.03	0.04	0.05	0.01	0.00	0.70	0.71	0.72
K	0.01	0.01	0.01	0.01	0.00	0.00	0.00	0.00	0.00	1.70	1.85	1.85	1.83	1.95	1.92	1.92	0.00	0.00	0.02	0.01	0.01
F	n.d.	n.d.	n.d.	n.d.	n.d.	n.d.	n.d.	n.d.	n.d.	0.17	0.04	0.03	0.04	0.08	0.04	0.08	n.d.	n.d.	n.d.	n.d.	n.d.
Cl	n.d.	n.d.	n.d.	n.d.	n.d.	n.d.	n.d.	n.d.	n.d.	0.10	0.06	0.06	0.04	0.04	0.04	0.02	n.d.	n.d.	n.d.	n.d.	n.d.
Total cation	5.00	5.00	5.00	5.01	7.96	7.98	8.01	7.99	2.99	15.48	15.51	15.39	15.45	15.56	15.60	15.55	8.01	7.99	5.00	5.00	5.00
$Mg/(Fe_{total}+Mg)$					0.21	0.10	0.14	0.11	0.27	0.64	0.47	0.40	0.42	0.41	0.40	0.45	0.07	0.10			
An	37.0	33.0	31.0	25.7															28.2	28.3	26.8
$\log(f_{H2O}/f_{HCl})$ of fluid *1										3.65	3.94			4.24	4.28						
$\log(f_{H2O}/f_{HCl})$ of fluid *2										0.12	1.19			2.19	2.25						
$\log(f_{H2O}/f_{HF})$ of fluid *1										4.31	5.07			5.12	5.46						
Temperature (°C)										800 *4	700 *3			580 *3	580 *3						

sample	TK2009112601C						TK2009113001B											
mineral	Bt	Bt	Bt	Bt	Bt	Bt	Grt	Grt	Pl	Pl	Bt	Bt	Bt	Bt	Bt	Bt	Bt	Bt
occurrence	in matrix	in matrix	Bt-Pl intergrowth replacing Grt	Bt-Pl intergrowth replacing Grt	retrograde Bt next to Grt	crack-filling Bt in Grt	in matrix	in matrix	in matrix	Bt-Pl intergrowth replacing Grt	inclusion in Grt	inclusion in Grt	in matrix	in matrix	in matrix (near Grt)	Bt-Pl intergrowth replacing Grt	retrograde Bt next to Grt	crack-filling Bt in Grt
core/rim							core	rim	core						rim			
SiO_2	35.22	34.90	34.57	34.90	34.77	33.93	38.63	37.82	59.05	54.60	37.27	38.17	37.25	37.06	36.33	37.24	35.79	36.52
TiO_2	2.28	3.12	3.72	0.30	0.51	2.95	0.06	0.11	0.04	0.07	4.11	3.91	4.16	3.75	4.29	0.17	3.56	0.09
Al_2O_3	17.88	16.62	16.87	18.70	19.64	17.22	22.05	21.69	25.41	28.26	16.65	15.82	16.24	16.59	16.91	18.54	17.58	19.49
Cr_2O_3	0.04	0.01	0.03	0.04	0.00	0.00	0.00	0.00	0.00	0.04	0.00	0.04	0.01	0.03	0.02	0.05	0.00	0.02
FeO	27.96	31.02	31.10	28.37	27.47	29.95	32.35	33.11	0.05	0.33	15.95	17.35	20.95	21.62	22.84	19.80	22.46	21.06
ZnO	n.d.	n.d.	n.d.	n.d.	n.d.	n.d.	n.d.	n.d.	n.d.	n.d.	n.d.	n.d.	n.d.	n.d.	n.d.	n.d.	n.d.	n.d.
MnO	0.16	0.00	0.07	0.02	0.00	0.08	0.74	0.92	0.04	0.02	0.00	0.00	0.00	0.00	0.00	0.00	0.00	0.18
MgO	4.47	3.74	2.97	4.52	3.41	3.76	4.70	2.99	0.01	0.00	12.61	12.77	9.24	9.44	9.14	12.12	8.82	11.30
CaO	0.00	0.03	0.01	0.11	0.02	0.04	3.45	4.48	7.48	11.12	0.05	0.01	0.00	0.01	0.00	0.04	0.00	0.05
BaO	0.13	0.06	0.12	0.00	0.00	0.17	0.00	0.01	0.00	0.09	0.34	0.13	0.14	0.13	0.17	0.00	0.00	0.00
Na_2O	0.05	0.04	0.03	0.08	0.04	0.09	0.00	0.02	7.34	5.24	0.08	0.12	0.10	0.08	0.04	0.05	0.02	0.06
K_2O	8.19	7.49	7.92	7.51	9.53	7.20	0.00	0.00	0.19	0.14	8.07	8.12	8.27	8.12	7.88	8.18	8.16	8.23
F	0.06	0.00	0.00	0.18	0.00	0.00	n.d.	n.d.	n.d.	n.d.	0.20	0.30	0.08	0.04	0.00	0.12	0.00	0.10
Cl	0.61	0.24	0.07	0.37	0.11	0.09	n.d.	n.d.	n.d.	n.d.	0.34	0.26	0.14	0.11	0.22	0.03	0.19	0.19
-O≡F	0.03	0.00	0.00	0.08	0.00	0.00	n.d.	n.d.	n.d.	n.d.	0.09	0.13	0.03	0.02	0.00	0.05	0.00	0.04
-O≡Cl	0.14	0.05	0.02	0.08	0.02	0.02	n.d.	n.d.	n.d.	n.d.	0.08	0.06	0.03	0.03	0.05	0.01	0.04	0.04
Total	96.87	97.22	97.45	94.94	95.47	95.46	101.98	101.14	99.62	99.91	95.52	96.79	96.50	96.93	97.77	96.28	96.54	97.20
number of O	22	22	22	22	22	22	12	12	8	8	22	22	22	22	22	22	22	22
Si	5.49	5.47	5.42	5.53	5.49	5.40	3.00	2.99	2.65	2.47	5.55	5.63	5.61	5.56	5.44	5.55	5.42	5.44
Ti	0.27	0.37	0.44	0.04	0.06	0.35	0.00	0.01	0.00	0.00	0.46	0.43	0.47	0.42	0.48	0.02	0.41	0.01
Al	3.29	3.07	3.12	3.49	3.66	3.23	2.02	2.02	1.34	1.51	2.92	2.75	2.88	2.93	2.99	3.26	3.14	3.42
Cr	0.01	0.00	0.00	0.01	0.00	0.00	0.00	0.00	0.00	0.00	0.00	0.01	0.00	0.00	0.00	0.01	0.00	0.00
Fe	3.65	4.07	4.08	3.76	3.63	3.99	2.10	2.19	0.00	0.01	1.99	2.14	2.64	2.71	2.86	2.47	2.85	2.62
Mn	0.02	0.00	0.01	0.00	0.00	0.01	0.05	0.06	0.00	0.00	0.00	0.00	0.00	0.00	0.00	0.00	0.00	0.02
Mg	1.04	0.87	0.69	1.07	0.80	0.89	0.54	0.35	0.00	0.00	2.80	2.81	2.07	2.11	2.04	2.69	1.99	2.51
Ca	0.00	0.00	0.00	0.02	0.00	0.01	0.29	0.38	0.36	0.54	0.01	0.00	0.00	0.00	0.00	0.01	0.00	0.01
Ba	0.01	0.00	0.01	0.00	0.00	0.01	0.00	0.00	0.00	0.00	0.02	0.01	0.01	0.01	0.01	0.00	0.00	0.00
Zn	n.d.	n.d.	n.d.	n.d.	n.d.	n.d.	n.d.	n.d.	n.d.	n.d.	n.d.	n.d.	n.d.	n.d.	n.d.	n.d.	n.d.	n.d.
Na	0.01	0.01	0.01	0.02	0.01	0.03	0.00	0.00	0.64	0.46	0.02	0.03	0.03	0.02	0.01	0.01	0.01	0.02
K	1.63	1.50	1.59	1.52	1.92	1.46	0.00	0.00	0.01	0.01	1.53	1.53	1.59	1.55	1.51	1.56	1.58	1.56
F	0.03	0.00	0.00	0.09	0.00	0.00	n.d.	n.d.	n.d.	n.d.	0.10	0.14	0.04	0.02	0.00	0.06	0.00	0.05
Cl	0.16	0.06	0.02	0.10	0.03	0.02	n.d.	n.d.	n.d.	n.d.	0.09	0.06	0.04	0.03	0.06	0.01	0.05	0.05
Total cation	15.41	15.38	15.37	15.46	15.58	15.38	7.99	8.00	5.00	5.01	15.31	15.34	15.29	15.33	15.34	15.58	15.39	15.63
$Mg/(Fe_{total}+Mg)$	0.22	0.18	0.15	0.22	0.18	0.18	0.21	0.14			0.59	0.57	0.44	0.44	0.42	0.52	0.41	0.49
An									35.6	53.6								
$\log(f_{H2O}/f_{HCl})$ of fluid *1			4.19	3.50	4.02						3.70	3.82				4.95	4.09	
$\log(f_{H2O}/f_{HCl})$ of fluid *2			2.02	1.14	1.76						0.31	0.47				2.32	1.74	
$\log(f_{H2O}/f_{HF})$ of fluid *1			–	4.26	–						4.52	4.33				5.17	–	
Temperature (°C)			760 *3	760 *3	760 *3						800 *4	800 *4				640 *3	640 *3	

	occurrence	zoning	$^{207}Pb/^{235}U$	error (± 2S.D.)	$^{206}Pb/^{238}U$	error (± 2S.D.)	Error correlation	$^{207}Pb/^{206}Pb$	error (± 2S.D.)	$^{207}Pb/^{235}U$ age (Ma)	error (± 2S.D., Ma)	$^{206}Pb/^{238}U$ age (Ma)	error (± 2S.D., Ma)	$^{207}Pb/^{206}Pb$ age (Ma)	error (± 2S.D., Ma)	Concnc ordance (%)	Th/U	U (ppm)	error (± 2S.D., ppm)	Th (ppm)	error (± 2S.D., ppm)	Pb (ppm)	error (± 2S.D., ppm)
TK20091126O1-51A	inc in garnet	core	0.788945	0.039112	0.095355	0.004257	0.901	0.060007	0.001293	591	22	587	25	604	47	101	0.08	3121	448	234	67	375	304
TK20091126O1-51B	inc in garnet	rim	0.762783	0.05415	0.092749	0.004298	0.653	0.059647	0.003208	576	32	572	25	591	121	101	0.19	322	46	60	17	39	32
TK20091126O1-51C	inc in garnet	mantle	0.782543	0.040865	0.092992	0.004169	0.859	0.061032	0.001634	587	24	573	25	640	59	102	0.07	1624	233	121	35	190	155
TK20091126O1-53A	in matrix	core	0.755302	0.038372	0.093941	0.004201	0.880	0.058313	0.001405	571	22	579	25	542	54	99	0.13	2270	326	292	84	272	221
TK20091126O1-53B	in matrix	rim	0.751175	0.048011	0.090952	0.004444	0.764	0.0599	0.002468	569	28	561	26	600	92	101	0.22	633	69	142	31	76	57
TK20091126O1-55A	in matrix	core	0.87678	0.050424	0.102448	0.004635	0.787	0.06207	0.002204	639	28	629	27	677	78	102	0.37	710	102	261	75	99	80
TK20091126O1-55B	in matrix	mantle	0.900365	0.074135	0.103273	0.004918	0.578	0.063231	0.004247	652	40	634	29	716	150	103	0.42	171	25	73	21	24	20
TK20091126O1-55C	in matrix	rim	0.815548	0.047895	0.09628	0.004364	0.772	0.061435	0.002294	606	27	593	26	654	82	102	0.11	678	97	76	22	84	68
TK20091126O1-56A	inc in garnet	rim	0.727565	0.058196	0.093144	0.004386	0.589	0.056652	0.003663	555	35	574	26	478	150	97	0.29	228	33	66	19	28	23
TK20091126O1-56B	inc in garnet	mantle	0.818644	0.042554	0.097995	0.004392	0.862	0.060589	0.001596	607	24	603	26	625	58	101	0.20	1624	233	321	92	208	169
TK20091126O1-57A	inc in garnet	core	0.766414	0.042563	0.09441	0.004254	0.811	0.058877	0.001911	578	25	582	25	563	72	99	0.28	1005	144	282	81	126	102
TK20091126O1-57B	inc in garnet	rim	0.742705	0.04776	0.091452	0.004183	0.711	0.058901	0.002662	564	28	564	25	563	102	100	0.23	482	69	112	32	58	47
TK20091126O1-61A	in matrix	rim	0.790243	0.048438	0.092562	0.002552	0.450	0.061919	0.00339	591	28	571	15	671	122	104	0.30	279	18	84	11	36	24
TK20091126O1-61B	in matrix	rim	0.927303	0.047488	0.09775	0.004369	0.875	0.068964	0.001711	666	25	600	26	898	52	111	0.10	1714	246	167	48	218	177
TK20091126O1-61C	in matrix	core	0.881333	0.058623	0.100217	0.004993	0.495	0.063781	0.005571	642	49	616	29	734	197	104	0.38	101	15	39	11	14	11
TK20091126O1-62A	in matrix	rim	0.799504	0.026226	0.094873	0.002312	0.743	0.061119	0.001342	597	15	584	14	643	48	102	0.05	2506	165	118	16	311	211
TK20091126O1-62B	in matrix	mantle	0.773234	0.06798	0.095387	0.002997	0.357	0.058792	0.004827	582	40	587	18	559	190	99	0.37	122	8	45	6	16	11
TK20091126O1-62C	in matrix	core	0.858849	0.046529	0.100255	0.002672	0.492	0.062131	0.002931	629	26	616	16	679	104	102	0.35	353	23	122	16	52	35
TK20091126O1-63A	in matrix	rim	0.763853	0.027361	0.09456	0.002327	0.687	0.058587	0.001525	576	16	582	14	552	58	99	0.16	1605	106	256	34	204	138
TK20091126O1-63B	in matrix	core	0.765639	0.033241	0.095455	0.002416	0.583	0.058173	0.002052	577	19	588	14	536	79	98	0.23	755	50	174	23	98	67
TK20091126O1-65	inc in garnet	mantle	0.799718	0.041597	0.096685	0.004641	0.923	0.05999	0.001201	597	24	595	27	603	44	100	0.08	4058	444	321	70	501	377
TK20091126O1-66	inc in garnet	core	0.828164	0.047665	0.10013	0.004445	0.841	0.059986	0.001869	613	27	615	28	603	69	100	0.36	1100	120	397	87	151	113
TK20091126O1-67	inc in garnet	core	0.804444	0.042348	0.096049	0.004615	0.913	0.060744	0.001306	599	24	591	27	630	47	101	0.08	3161	346	241	53	388	292
TK20091126O1-68A	in garnet b.d.	core	0.747001	0.052567	0.091847	0.004535	0.702	0.058987	0.002958	566	31	566	27	567	113	100	0.25	413	45	102	22	51	38
TK20091126O1-68B	inc in garnet	rim	0.757836	0.05665	0.092957	0.004625	0.666	0.059128	0.003299	573	33	573	27	572	126	100	0.41	324	36	132	29	42	32
TK20091126O1-69	in matrix	mantle	0.873261	0.048714	0.103873	0.005014	0.865	0.060973	0.001705	637	27	637	29	638	61	100	0.37	1371	150	511	112	196	148
TK20091126O1-70A	inc in garnet	mantle	0.772304	0.041242	0.094678	0.004553	0.901	0.059161	0.001373	581	24	583	27	573	51	100	0.05	2593	284	140	31	311	234
TK20091126O1-70B	inc in garnet	core	0.809203	0.071248	0.096415	0.004928	0.581	0.060871	0.004364	602	41	593	29	635	162	101	0.33	180	20	60	13	24	18
TK20091126O1-70C	inc in garnet	rim	0.751315	0.044851	0.09158	0.004445	0.813	0.0595	0.002068	569	26	565	26	585	77	101	0.24	933	102	220	48	114	86
TK20091126O1-71A	in garnet b.d.	mantle	0.737393	0.079665	0.089201	0.004756	0.493	0.059955	0.005635	561	48	551	28	602	218	102	0.28	113	12	32	7	14	11
TK20091126O1-71B	in garnet b.d.	core	0.772689	0.042369	0.094535	0.004556	0.879	0.05928	0.001551	581	25	582	27	577	58	100	0.31	1846	202	570	125	236	177
TK20091126O1-73	inc in garnet	core	0.789002	0.041562	0.095802	0.004603	0.912	0.059731	0.00129	591	24	590	27	594	47	100	0.08	3179	348	258	56	390	293
TK20091126O1-74	in matrix	mantle	0.764374	0.033423	0.09309	0.002748	0.675	0.059552	0.001921	577	19	574	16	587	72	100	0.05	2454	231	124	23	297	206
TK20091126O1-75A	in matrix	mantle	0.743313	0.035873	0.090293	0.002703	0.620	0.059706	0.00226	564	21	557	16	593	84	101	0.10	1253	118	129	24	149	103
TK20091126O1-75B	in matrix	rim	0.769999	0.047878	0.094104	0.002958	0.505	0.059345	0.003184	580	28	580	17	580	121	100	0.24	423	40	102	19	54	38
TK20091126O1-75C	in matrix	rim	0.754307	0.043921	0.090164	0.002796	0.533	0.060675	0.00299	571	26	557	17	628	110	103	0.33	542	51	180	34	68	47
TK20091126O1-76A	inc in garnet	core	0.905963	0.043657	0.112273	0.004536	0.621	0.058524	0.00221	655	24	686	26	549	85	95	0.10	1035	97	108	20	153	106
TK20091126O1-76B	inc in garnet	rim	0.777846	0.032673	0.095762	0.002812	0.699	0.058911	0.001769	584	19	590	17	564	67	99	0.06	3758	354	242	45	469	325
TK20091126O1-77A	in matrix	rim	0.729311	0.05081	0.092435	0.002981	0.463	0.057224	0.003534	556	30	570	18	500	142	98	0.25	314	30	78	15	40	28
TK20091126O1-77B	in matrix	mantle	0.857035	0.068791	0.102049	0.00346	0.422	0.06091	0.004431	629	38	626	20	636	165	100	0.35	183	17	65	12	27	18
TK20091126O1-77C	in matrix	core	0.869925	0.036949	0.103534	0.003046	0.693	0.060939	0.001867	636	20	635	18	637	67	100	0.42	2933	276	1228	231	432	300
TK20091126O1-78A	in matrix	core	0.921466	0.066634	0.11078	0.003632	0.453	0.060328	0.003888	663	36	677	21	615	146	98	0.52	225	21	117	22	36	25
TK20091126O1-78B	in matrix	mantle	1.462504	0.059643	0.123014	0.003608	0.719	0.086227	0.002443	915	25	748	21	1343	56	122	0.10	3424	322	355	67	588	408
TK20091126O1-78C	in matrix	rim	0.741325	0.041328	0.093509	0.002867	0.550	0.057498	0.002677	563	24	576	17	511	106	98	0.20	645	61	129	24	81	56
TK20091130O1B-11A	in matrix	core	1.33761	0.11176	0.151423	0.004179	0.346	0.064067	0.005022	862	50	909	25	744	175	94.9	0.54	93	12	50	13	21	14
TK20091130O1B-11B	in matrix	rim	0.778667	0.035572	0.093726	0.002105	0.492	0.060254	0.002397	585	21	578	12	613	88	101	0.05	773	96	41	10	96	62
TK20091130O1B-12A	inc in garnet	rim	0.794271	0.059338	0.098115	0.002616	0.357	0.058713	0.004097	594	34	603	15	556	160	98	1.12	199	25	223	55	33	21
TK20091130O1B-12B	inc in garnet	mantle	0.813669	0.029937	0.096636	0.002074	0.583	0.061067	0.001825	605	17	595	12	642	66	102	0.05	1786	222	90	22	230	148
TK20091130O1B-12C	inc in garnet	core	1.106515	0.065009	0.122958	0.003017	0.418	0.065268	0.003484	756	32	748	17	783	116	101	0.46	263	33	122	30	48	31
TK20091130O1B-17D	inc in garnet	rim	0.737288	0.073081	0.09493	0.00345	0.367	0.056329	0.005194	561	44	585	20	465	218	95.9	1.29	125	12	161	30	20	14
TK20091130O1B-21A	in inc biotite	mantle	1.227391	0.050707	0.133708	0.002953	0.535	0.066577	0.002325	813	23	809	17	825	75	101	0.48	714	89	344	85	141	91
TK20091130O1B-21B	in inc biotite	core	1.158487	0.050569	0.127369	0.002849	0.512	0.065967	0.002473	781	24	773	16	805	81	101	0.69	615	76	426	106	121	78
TK20091130O1B-21C	inc in biotite	rim	0.700768	0.050331	0.094408	0.002437	0.359	0.053835	0.003608	539	31	582	14	364	159	92.7	1.01	246	31	247	61	38	25
TK20091130O1B-22A	in matrix	rim	0.811972	0.068571	0.097048	0.002769	0.338	0.060681	0.004823	604	39	597	16	628	181	101	1.10	148	18	162	40	25	16
TK20091130O1B-22B	in matrix	mantle	0.786791	0.035351	0.099857	0.002227	0.496	0.057145	0.002229	589	20	614	13	497	88	96.1	0.09	804	100	71	18	108	70
TK20091130O1B-23A	inc in garnet	rim	0.846684	0.062113	0.096741	0.002593	0.365	0.063476	0.004335	623	35	595	15	724	152	104.6	0.96	197	24	190	47	31	20
TK20091130O1B-23B	inc in garnet	core	1.003796	0.040556	0.115087	0.002521	0.542	0.063258	0.002148	706	21	702	15	717	74	101	0.31	947	118	297	74	155	100
TK20091130O1B-27A	in matrix	rim	1.153538	0.045532	0.12762	0.002787	0.553	0.065556	0.002156	779	22	774	16	792	71	101	0.12	913	113	112	28	159	102
TK20091130O1B-27B	in matrix	core	1.282152	0.070143	0.133094	0.003718	0.511	0.069868	0.003286	838	32	805	21	924	100	104.0	0.20	277	31	57	13	51	31
TK20091130O1B-27C	in matrix	mantle	1.202825	0.04595	0.136023	0.00352	0.677	0.064134	0.001802	802	21	822	20	746	61	97.5	0.04	1225	137	51	12	221	133
TK20091130O1B-2A	core	core	1.108003	0.061442	0.124212	0.003348	0.486	0.064696	0.003135	757	30	755	19	764	106	100	0.58	259	17	151	20	48	32
TK20091130O1B-2B	in matrix	rim	0.818233	0.054712	0.095602	0.002713	0.424	0.062074	0.003758	607	31	589	16	677	135	103.1	0.17	218	14	38	5	28	19
TK20091130O1B-2C	in matrix	mantle	1.103481	0.045407	0.126742	0.003193	0.612	0.063146	0.002054	755	22	769	18	713	71	98	0.28	637	42	179	24	112	76
TK20091130O1B-3A	in matrix	rim	0.71351	0.041963	0.089294	0.002416	0.460	0.057953	0.003026	547	25	551	14	528	119	99	0.38	340	22	130	17	43	29
TK20091130O1B-3B	in matrix	mantle	0.947184	0.033726	0.11128	0.00274	0.692	0.061733	0.001588	677	18	680	16	665	56	99	0.04	1342	89	54	7	195	132
TK20091130O1B-3C	in matrix	core	1.163294	0.055279	0.12822	0.00333	0.547	0.065801	0.002618	784	26	778	19	800	86	101	0.57	381	25	216	29	72	49
TK20091130O1B-4A	in matrix	core	1.266264	0.061775	0.14071	0.003806	0.555	0.065268	0.00265	831	28	849	22	783	88	98	0.41	399	45	163	37	81	48
TK20091130O1B-4B	in matrix	rim	0.788545	0.063174	0.097343	0.003019	0.387	0.058752	0.00434	590	37	599	18	558	170	99	1.51	163	18	246	55	29	17
TK20091130O1B-5A	in matrix	mantle	1.050245	0.061287	0.118741	0.00335	0.483	0.064149	0.003277	729	31	723	19	747	112	101	0.64	277	31	178	40	50	30
TK20091130O1B-5B	in matrix	core	1.262501	0.075225	0.139266	0.003844	0.463	0.065749	0.003472	829	34	841	22	798	115	99	0.49	189	13	92	12	39	26
TK20091130O1B-7A	in matrix	rim	0.784725	0.047907	0.096393	0.00273	0.464	0.059043	0.003193	588	28	593	16	569	122	99	0.85	324	36	276	62	50	30
TK20091130O1B-7B	in matrix	core	1.136167	0.044608	0.12721	0.003305	0.662	0.064777	0.001907	771	21	772	19	767	63	100	0.13	1108	124	140	31	191	115
TK20091130O1B-7C	in matrix	rim	0.80033	0.050941	0.09914	0.00284	0.450	0.058549	0.003328	597	29	609	17	550	129	98	0.94	284	32	267	60	45	27
TK20091130O1B-8A	in matrix	rim	0.767331	0.060032	0.09714	0.002974	0.391	0.05729	0.004125	578	35	598	17	503	167	96.8	0.96	176	20	169	38	28	17
TK20091130O1B-8B	in matrix	core	0.983365	0.061772	0.110959	0.003198	0.459	0.064276	0.003588	695	32	678	19	751	123	102.5	0.28	242	27	67	15	38	23
TK20091130O1B-9A	inc in garnet	core	1.171108	0.066864	0.124656	0.003515	0.494	0.068137	0.003383	787	32	757	20	873	106	103.9	0.61	267	30	162	36	51	30
TK20091130O1B-9B	in matrix	mantle	1.187953	0.044968	0.133414	0.003448	0.683	0.06458	0.001786	795	21	807	20	761	59	98	0.43	1314	147	562	126	255	153
TK20091130O1B-9C	in matrix	rim	1.141784	0.046374	0.130672	0.003411	0.643	0.063372	0.001972	773	22	792	19	721	67	97.7	0.11	922	103	97	22	162	97
TK20113001G 10-1	inc in garnet	rim	0.899376	0.051048	0.099993	0.004146	0.730	0.065233	0.002529	651	28	614	24	782	84	106	0.06	567	82	33	5	57	9
TK20113001G 10-2	inc in garnet	rim	1.022433	0.045106	0.094269	0.003822	0.919	0.078662	0.001368	715	23	581	23	1164	35	123	0.02	2706	390	52	8	262	40
TK20113001G 10-3	inc in garnet	mantle	1.053029	0.039198	0.112614	0.002590	0.618	0.067818	0.001985	730	20	688	15	863	62	106	0.05	493	143	23	5	54	15
TK20113001G 1-1	in matrix	rim	0.865671	0.039148	0.103290	0.002303	0.493	0.060785	0.002391	633	22	634	13	632	87	100	0.01	1202	155	13	2	119	16
TK20113001G 1-2	in matrix	rim	0.873669	0.040272	0.101982	0.002286	0.486	0.062133	0.002503	638	22	626	13	679	88	102	0.01	1064	137	11	1	104	14
TK20113001G 2-1	in matrix	mantle	0.886832	0.044025	0.102939	0.004207	0.823	0.062483	0.001760	645	24	632	25	691	61	102	0.00	1105	159	4	1	111	17
TK20113001G 2-2	inc in garnet	core	0.908821	0.046630	0.106331	0.004359	0.799	0.061989	0.001913	656	25	651	25	674	67	101	0.00	893	129	1	0	93	14
TK20113001G 2-4	inc in garnet	rim	0.968519	0.035503	0.094355	0.002173	0.628	0.074446	0.002123	688	18	581	13	1054	59	118	0.07	569	165	42	9	54	15
TK20113001G 2-5	inc in garnet	rim	0.865268	0.031424	0.095150	0.001956	0.566	0.065954	0.001975	633	17	586	12	805	64	108	0.07	523	61	38	4	49	6
TK20113001G 7-1	inc in garnet	rim	0.740215	0.027448	0.092413	0.002109	0.615	0.058093	0.001698	563	16	570	12	533	65	99	0.05	697	202	35	7	62	17
TK20113001G 7-2	inc in garnet	mantle	1.010486	0.033706	0.116285	0.002624	0.676	0.063024	0.001548	709	17	709	15	709	53	100	0.05	736	213	34	7	82	22
TK20113001G 7-3	inc in garnet	core	1.757276	0.122457	0.166619	0.004696	0.404	0.076492	0.004875	1030	46	993	26	1108	133	104	0.38	61	18	24	5	11	3
TK20113001G 7-4	in matrix	rim	0.937309	0.029901	0.095983	0.001923	0.632	0.071260	0.001762	671	16	587	11	965	51	114	0.04	723	84	28	3	68	8
TK20113001G 8-1	in matrix	rim	1.821724	0.045807	0.195963	0.003953	0.741	0.062307	0.002331	609	26	589	23	685	82	103	-	266	96	-	-	63	10
TK20113001G 8-2	inc in garnet	core	2.070687	0.091097	0.188508	0.007644	0.922	0.079668	0.001360	1139	31	1113	42	1189	34	102	0.26	1395	201	366	54	279	43
TK20113001G2 111-1	in garnet b.d.	mantle	1.539872	0.047903	0.147966	0.003120	0.678	0.075478	0.001726	946	19	890	18	1081	47	106	0.18	1204	124	221	16	188	18
TK20113001G2 111-2	in garnet b.d.	rim	0.784291	0.034890	0.097972	0.002183	0.501	0.058060	0.002236	588	20	603	13	532	87	98	0.04	699	72	30	2	68	7
TK20113001G2 111-3	in garnet b.d.	rim	0.747601	0.033970	0.094491	0.002114	0.492	0.057382	0.002270	567	20	582	12	506	89	97	0.09	692	71	63	4	66	6
TK20113001G2 112	inc in biotite	core	1.308895	0.059958	0.116030	0.002689	0.506	0.081815	0.003233	850	27	708	16	1241	79	120	0.16	406	42	64	5	50	5
TK20113001G2 113-1	in matrix	core	1.881409	0.054977	0.184617	0.003855	0.715	0.073911	0.001511	1075	20	1092	21	1039	42	98	0.33	1321	136	437	31	265	26
TK20113001G2 113-2	in garnet b.d.	rim	1.853040	0.075884	0.183856	0.004104	0.545	0.073098	0.002510	1065	27	1088	22	1017	71	98	0.18	386	40	69	5	74	7
TK20113001G2 139-1	in garnet b.d.	core	0.765100	0.029278	0.093823	0.002027	0.565	0.059144	0.001868	577	17	578	12	572	70	100	0.02	1110	114	23	2	103	10
TK20113001G2 139-2	in garnet b.d.	rim	0.974806	0.043874	0.095660	0.002181	0.507	0.073907	0.002868	691	23	589	13	1039	80	117	0.07	562	58	41	3	56	6
TK20113001G2 139-3	in garnet b.d.	mantle	1.157245	0.036667	0.112158	0.002370	0.667	0.074833	0.001767	781	17	685	14	1064	48	114	0.03	1478	152	47	3	172	17
TK20113001G2 14-1	in garnet	core	1.491455	0.061276	0.151684	0.005733	0.920	0.071313	0.001148	927	25	910	32	966	33	102	0.24	5099	416	1242	129	835	73
TK20113001G2 14-2	inc in garnet	rim	0.909514	0.046307	0.106493	0.004102	0.757	0.061942	0.002062	657	25	652	24	672	73	101	0.03	913	74	23	2	98	9
TK20113001G2 175-1	inc in sillimanite	core	1.490070	0.042759	0.153073	0.003183	0.725	0.070600	0.001396	926	18	918	18	946	41	101	0.09	1820	187	161	11	283	27
TK20113001G2 175-2	inc in sillimanite	mantle	0.769230	0.027397	0.093321	0.001992	0.599	0.059783	0.001704	579	16	575	12	596	63	101	0.04	1395	144	54	4	130	13
TK20113001G2 175-3	inc in sillimanite	rim	0.801347	0.041700	0.093132	0.002179	0.450	0.062405	0.002901	598	24	574	13	688	102	104	0.09	465	47	40	3	43	4
TK20113001G2 18-1	in garnet b.d.	core	1.207844	0.064420	0.132689	0.005225	0.738	0.066020	0.002375	804	30	803	30	807	77	100	0.13	625	60	79	3	87	8
TK20113001G2 18-2	in garnet b.d.	mantle	0.788112	0.040719	0.093454	0.003660	0.758	0.061163	0.002061	590	23	576	22	645	74	102	0.05	1136	109	56	2	108	10
TK20113001G2 18-3	in garnet b.d.	rim	0.794864	0.049268	0.093924	0.003764	0.646	0.061379	0.002903	594	28	579	22	653	105	103	0.04	484	46	22	1	46	4
TK20113001G2 182-1	inc in sillimanite	core	2.055492	0.057176	0.188102	0.003903	0.746	0.079254	0.001468	1134	19	1111	21	1178	37	102	1.11	1835	337	2029	347	432	86
TK20113001G2 184-1	inc in garnet overgrowing sillimanite	core	1.860032	0.072533	0.181679	0.004006	0.566	0.074253	0.002388	1067	26	1076	22	1048	66	99	0.40	506	93	201	34	103	20
TK20113001G2 184-2	inc in garnet overgrowing sillimanite	core	1.495085	0.069447	0.155541	0.003569	0.494	0.069714	0.002816	928	29	932	20	920	85	100	0.25	381	70	94	16	64	13
TK20113001G2 184-3	inc in garnet overgrowing sillimanite	rim	0.808067	0.046032	0.091987	0.002220	0.424	0.063712	0.003288	601	26	567	13	732	113	106	0.20	417	76	85	15	41	8
TK20113001G2 184-4	inc in garnet overgrowing sillimanite	mantle	1.294331	0.059205	0.098875	0.002320	0.513	0.094942	0.003728	843	27	608	14	1527	76	139	0.19	479	88	91	16	54	11
TK20113001G2 184-5	inc in garnet overgrowing sillimanite	core	1.675727	0.079980	0.167780	0.003899	0.487	0.072437	0.003020	999	31	1000	22	998	87	100	0.28	318	58	88	15	57	11
TK20113001G2 192-1	in garnet b.d.	core	1.651633	0.040849	0.156999	0.003206	0.826	0.076298	0.001064	990	16	940	18	1103	28	105	0.12	6366	1167	766	131	1050	209
TK20113001G2 192-2	in garnet b.d.	mantle	0.823632	0.029384	0.099030	0.002114	0.598	0.060321	0.001724	610	16	609	12	615	63	100	0.05	1475	270	68	12	147	29
TK20113001G2 192-3	in garnet b.d.	rim	0.791947	0.039698	0.091759	0.002121	0.461	0.062596	0.002784	592	23	566	13	695	98	105	0.10	581	107	60	10	55	11
TK20113001G2 194